Application of H_2N-Fe_3O_4 and $NaDyF_4$-$NaGdF_4$ Contrast Agents for the Early Detection of Prostate Cancer and Breast Cancer in the Animal Models

David MacDonald

Supervisor:

Dr. hab Barbara Błasiak, Institute of Nuclear Physics, Polish Academy of Sciences

A thesis submitted in fulfilment

of the requirements for the degree of

Doctor of Philosophy

at the

Henryk Niewodniczański Institute of Nuclear Physics

Polish Academy of Sciences

Kraków 2025

Acknowledgments

I would like to begin by expressing my deepest gratitude to Dr. hab Barbra Błasiak. This thesis would not have been possible without their guidance and support. I am profoundly thankful for the opportunity to engage in numerous fascinating interdisciplinary projects as a PhD student at the Henryk Niewodniczański Institute of Nuclear Physics, Polish Academy of Sciences.

I am also sincerely grateful to Prof. dr hab. Bogusław Tomanek, Dr. Fong-Yu Cheng and Prof. Frank van Veggel, for synthesizing the contrast agents studied in this thesis, to Prof. Danuta Kruk for including me in her research project, the many insightful discussions, and assistance with result interpretation, and to Dr. Krzysztof Jasiński for his invaluable help with experiments and overcoming technical challenges.

My heartfelt thanks go to all my colleagues from the Department of Magnetic Resonance Imaging for their unwavering support and for fostering a welcoming and collaborative atmosphere throughout my studies.

Finally, I would like to express my deepest appreciation to my friends and family, for being my greatest source of support and inspiration. This couldn’t be done without you.

Table of Contents

List of Acronyms

CA(s) – Contrast Agent(s)

EPR – Enhanced Permeability and Retention

FID – Free Induction Decay

FISP - Fast Imaging with Steady-state Precession

FOV – Field of View

IR – Inversion Recovery

MS- Multi Slice

ME – Multi-Echo

MRI – Magnetic Resonance Imaging

NMR – Nuclear Magnetic Resonance

NP(s) – Nanoparticle(s)

RARE – Rapid Acquisition with Relaxation Enhancement

RC – Relative Change

RF – Radio Frequency

ROI – Region of Interest

SE – Spin Echo

SPION -Superparamagnetic Iron Oxide Nanoparticle

SNR – Signal to Noise Ratio

T_1w – T_1-weighted

T_2w – T_2-weighted

TC – Tumor Contrast

TE – Echo Time

TEM – Transmission Electron Microscopy

TI – Inversion Time

TR – Repetition Time

XRD – X-ray Diffraction

GEMM – Genetically Engineered Mouse Model

CT – Computed Tomography

PSMA – Prostate Specific Membrane Antigen

HER2 - Human Epidermal Growth Factor Receptor 2

TNB – Triple Negative Breast

EPI – Echo Planar Imaging

EMF – Electromagnetic Force

CSF – Cerebrospinal Fluid

PEG – Polyethylene Glycol

ICP – Inductively Coupled Plasma

Summary

This thesis explores the application of contrast agents comprising paramagnetic nanoparticles, H_2N-Fe_3O_4 and $NaDyF_4$-$NaGdF_4$, to improve the early detection of prostate and breast cancer using a 9.4T magnetic resonance imaging (MRI) system. The relaxivity of H_2N-Fe_3O_4 in an aqueous solution was measured at the magnetic field of 9.4T for pre-clinical investigation as well as at 3T considering possible future clinical applications of the contrasts. Both nanoparticles were applied *in vivo* in prostate and breast cancer mouse models. The results showed that both contrast agents H_2N-Fe_3O_4 and $NaDyF_4$-$NaGdF_4$ significantly enhance tumor contrast 12 min and 15 min post injection respectively at 9.4T. The relaxivity measurements at 3T showed that the nanoparticles could also be effective in clinical settings.

In addition to the *in vivo* studies of the contrast agents, a theoretical MRI model comprising tumor and normal tissue was developed to investigate how image post-processing may further improve the tumor contrast in MRI. The model showed that subtraction of T_2-weighted from T_1-weighted image improves tumor contrast in MR images before and after injection of a contrast agent. The results were applied to *in vivo* MR images showing the expected tumor contrast improvement.

Overview

This thesis comprises ten chapters, each detailing a specific aspect of the research, including the theory, methodology and results. The structure is as follows:

Chapter 1 provides an overview of the fundamental principles of the Nuclear Magnetic Resonance (NMR). Chapter 2 explains the major hardware components of an MRI system and provides details of the signal acquisition and data processing in MRI, including Fourier Transform and k-space. It also presents various MRI pulse sequences, their parameters and image weighting hence image contrast and resolution. Chapter 3 introduces the T_1 and T_2 type contrast agents, targeted contrast agents and outlines current clinical approaches to prostate and breast cancer detection. Chapter 4 presents the animal models used in the thesis, synthesis of the contrast agents (H_2N-Fe_3O_4 and $NaDyF_4$-$NaGdF_4$), MRI acquisition protocols and image post-processing. Chapter 5 includes the results of the relaxivity measurements, *in vivo* MRI of prostate and breast cancer models, as well as post-processing techniques. Chapter 6 discusses the results and provides conclusions considering potential suitability of the agents in cancer imaging. Chapter 7 considers possible advances of the research, including improving contrast agent formulations, developing targeted agents as well as their potential applications in clinical MRI.

Chapter 1 Nuclear Magnetic Resonance

1.1 Introduction to NMR

NMR phenomenon is non-destructive and is used for determining the structure and dynamics of various biological molecules. The method requires placing a sample in the external magnetic field ($\vec{B}_0$) and applying variable radiofrequency (RF) field.

1.2 Nuclear Magnetic Moment and Larmour Precession

In NMR, the behavior of a nucleus in a magnetic field is characterized by the nuclear magnetic moment $\vec{\mu}$, which is directly proportional to its angular momentum $\vec{J}$, according to the equation [1]:

$$\vec{\mu} = \gamma \vec{J} \qquad 1.0$$

where γ is the gyromagnetic ratio, a particle specific (γ for protons = 2.675 x 10^8 rad/s/T), $\vec{J}$ is the angular momentum. Quantum mechanics states that the z-component (in the direction of $\vec{B}_0$) of the angular momentum is quantized. Therefore it can take on discrete values described by [1]:

$$J_z = \frac{m\,h}{2\pi} \qquad 1.1$$

where m is the magnetic quantum number, m = -I, -I+1, …, 0, …, I-1 and I is the spin quantum number. The spin quantum number I may have values of zero, integer and half integer and depends on the particle of interest [2].

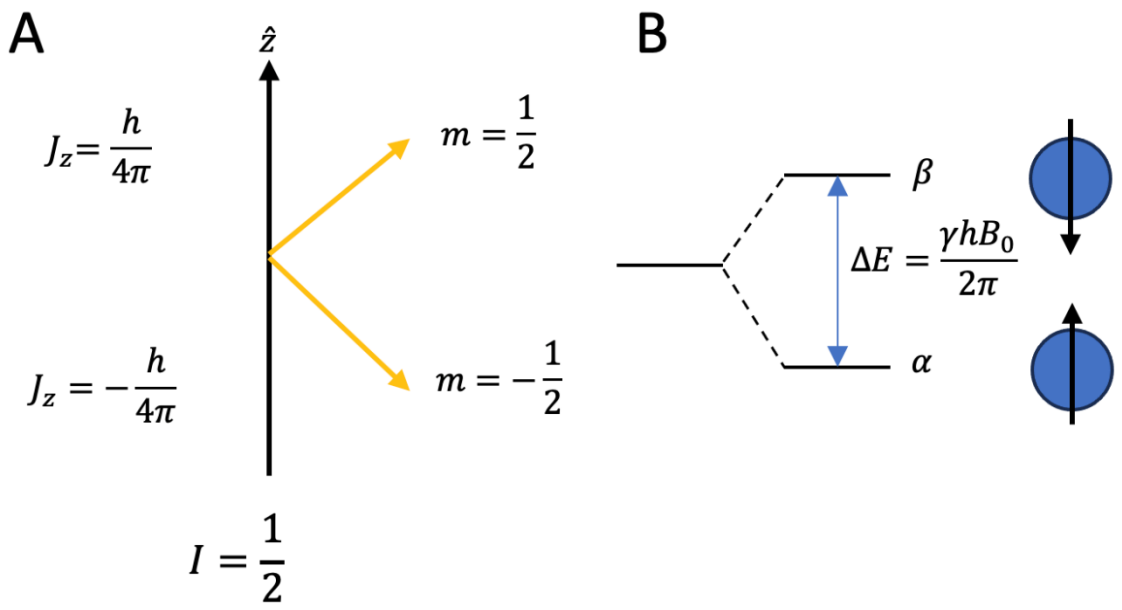

Fig. 1. *(A) A nuclei with spin quantum number I = ½. The two distinct values correspond to two discrete energy levels of the spin (m = - ½ and m = ½) when placed in the magnetic field. (B) Energy difference between the two states.*

For fermions, such as electrons or protons, with $I = \frac{1}{2}$, m can have only two values $m = \frac{1}{2}$, or $m = -\frac{1}{2}$. This leads to two distinct energy levels in the presence of the external magnetic field $\vec{B}_0$ described by the following equation [1]:

$$E_{pot} = -\vec{\mu} \cdot \vec{B}_0 = -\gamma \vec{J} \cdot \vec{B}_0 \qquad 1.2$$

where the energy difference between the two states α and β $m = \pm \frac{1}{2}$ in the external magnetic field B_0 is [1]:

$$\Delta E = \frac{\gamma h B_0}{2\pi} \qquad 1.3$$

The magnitude of the magnetic moment associated with the spin *I* can be expressed as [3]:

$$\mu = \gamma\hbar\sqrt{I(I+1)} \qquad 1.4$$

where $\hbar = \frac{h}{2\,\pi}$, and h is Plank's constant. When nuclei with non-zero magnetic moments are placed within a magnetic field $\vec{B}_0$ they precess around the $\vec{B}_0$ field with a characteristic frequency called the Larmour frequency (ω_0), as shown in Figure 2. The Larmour frequency depends on the nuclei of interest and strength of the applied magnetic field $\vec{B}_0$ [1]:

$$\vec{\omega}_0 = -\gamma\vec{B}_0 \qquad 1.5$$

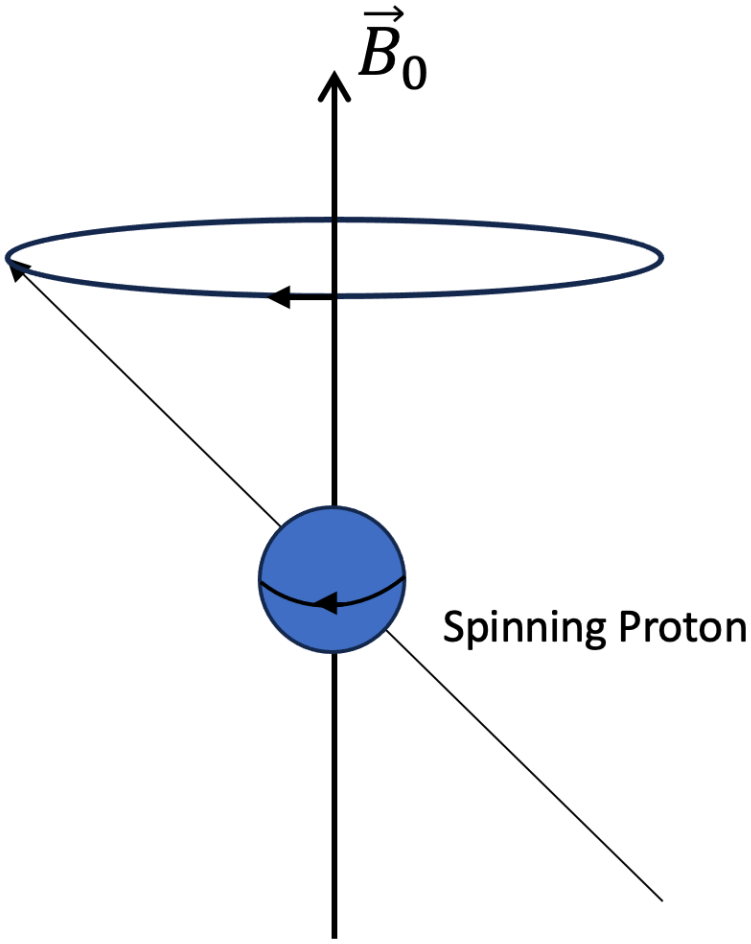

Fig. 2. *The precession of a proton in the external magnetic field.*

Because the energy state for $m = \frac{1}{2}$ (β state, aligned with the $\vec{B}_0$ field) is lower than that of $m = -\frac{1}{2}$ (α state, aligned against the $\vec{B}_0$ field), there is a net difference (more nuclei is aligned with the $\vec{B}_0$ field rather than against it). This slight excess in the $m = \frac{1}{2}$ state creates a net magnetization in a sample comprising hydrogen atoms (protons). The ratio of spin up compared to spin down population is described by the Boltzmann equation [3]:

$$\frac{N_-}{N_+} = \frac{\Delta \mathrm{E}}{kT} = \frac{\gamma \hbar B_0}{kT} \tag{1.6}$$

where T is the temperature in Kelvin and $k = 1.381\ x\ 10^{-23} JK^{-1}$ is the Boltzmann constant. The sum of magnetic moments placed in the magnetic field results in a net magnetization $\vec{M}$ in the direction of $\vec{B}_0$ [3]:

$$\vec{M} = \sum_{n=1}^{N_s} \vec{\mu}_n \tag{1.7}$$

where $\vec{\mu}_n$ is the magnetic moment of the individual nuclei, N_s is the number of spins (nuclei) and $\vec{M}$ is the net magnetization in the direction of $\vec{B}_0$.

Due to the population difference in spin states and the high natural abundance of water in biological samples makes ^{1}H suitable for MR imaging.

1.3 Bloch Equations

The Bloch equations describe the behaviour of magnetization (created by protons or unpaired electrons) in the external magnetic field $\vec{B}_0$. The nuclear and electron gyromagnetic factors are [1]:

$$\gamma_I = g_I \frac{e}{2\, m_p} \tag{1.8}$$

$$\gamma_S = g_e \frac{e}{2\, m_e} \tag{1.9}$$

where $e = 1.6\ x\ 10^{-19}C$ is the elementary charge of an electron, m_p and m_e are the proton and electron masses, g_e and g_I are Lande factors that depend on the particle, the proton gyromagnetic factor is $\gamma_I = \gamma_H = 2.68x10^8 T^{-1}s^{-1}$ and the electron gyromagnetic factor is $\gamma_S = 658.2\ \gamma_H$. The nuclear magneton and the electron Bohr magneton can be expressed as [1]:

$$\mu_n = \frac{e\ \hbar}{2\ m_p} \tag{1.10}$$

$$\mu_B = \frac{e\ \hbar}{2\ m_e} \tag{1.11}$$

The electrons and protons magnetic moments μ_s and μ_I, respectively can be expressed as [4]:

$$\mu_I = g_I \frac{e\ \hbar}{2\ m_p} \sqrt{I(I+1)} = \gamma_I \sqrt{I(I+1)} \tag{1.12}$$

$$\mu_s = g_e \frac{e\ \hbar}{2\ m_e} \sqrt{S(S+1)} = \gamma_S \sqrt{S(S+1)} \tag{1.13}$$

where S and I are the spins of the electron and proton respectively.

Considering the macroscopic case, when nuclei are placed in an external magnetic field $\vec{B}_0$, the net magnetization of both electrons (M_S) and nuclei (M_I) is oriented in the direction of $\vec{B}_0$ and can be expressed as [4]:

$$M_I = \frac{N\gamma_I^2 \hbar^2 B_0}{3\ k_b T} I(I+1) \tag{1.14}$$

$$M_S = \frac{N\gamma_S^2 \hbar^2 B_0}{3\ k_b T} S(S+1) \tag{1.15}$$

where N is the number of nuclei per unit volume, $k_b = 1.38x10^{-23}m^2kgs^{-2}K^{-1}$ is the Boltzmann constant, and T is temperature.

The nuclei magnetization $\vec{M}$ undergoes Larmour precession in the magnetic field $\vec{B}_0$. This precession is described by the Bloch equation [1]:

$$\frac{d\,\vec{M}(t)}{dt} = \gamma\vec{M}(t) \times \vec{B}_0 \qquad 1.16$$

Since $\vec{M} = [M_x, M_y, M_z]$, the equation for the components of the magnetization $\vec{M}$ becomes [4]:

$$\frac{dM_x(t)}{dt} = \gamma\left[\vec{M}(t) \times \vec{B}_0\right]_x \qquad 1.17$$

$$\frac{d\,M_y(t)}{dt} = \gamma\left[\vec{M}(t) \times \vec{B}_0\right]_y \qquad 1.18$$

$$\frac{d\,M_z(t)}{dt} = \gamma\left[\vec{M}(t) \times \vec{B}_0\right]_z \qquad 1.19$$

By expanding the curl operator, the equations then become [4]:

$$\frac{d\,M_x(t)}{dt} = \gamma\left[M_y(t)B_z - M_z(t)B_y\right] \qquad 1.20$$

$$\frac{d\,M_y(t)}{dt} = \gamma[M_z(t)B_x - M_x(t)B_z] \qquad 1.21$$

$$\frac{d\,M_z(t)}{dt} = \gamma\left[M_x(t)B_y - M_y(t)B_x\right] \qquad 1.22$$

To simplify the above equations we can assume the magnetic field is only in the $\hat{z}$ direction, such that $\vec{B} = [0,0,B_0]$. In this case the equations become:

$$\frac{dM_{\perp}(t)}{dt} = -i\gamma B_0 M_{\perp} \tag{1.23}$$

$$\frac{dM_Z(t)}{dt} = 0 \tag{1.24}$$

where $M_{\perp} = M_x + iM_y$ is the transverse magnetization, such that:

$$M_x(t) = \sqrt{M_x^2(0) + M_y^2(0)}\cos(\gamma B_0 t) \tag{1.25}$$

$$M_y(t) = -\sqrt{M_x^2(0) + M_y^2(0)}\sin(\gamma B_0 t) \tag{1.26}$$

$$M_z(t) = M_z(0) \tag{1.27}$$

1.4 Relaxation Processes

Due to relaxation processes the magnetization $\vec{M}$ in the external magnetic field $\vec{B}_0$ returns to its equilibrium following a perturbation. The relaxation processes include two mechanisms: longitudinal relaxation (T_1) and transverse relaxation (T_2). The transverse relaxation time cannot be longer than the longitudinal relaxation time, hence $T_2 \leq T_1$ [5]. Incorporating these relaxation processes, the Bloch equations can be modified as follows:

$$\frac{d\,M_x(t)}{dt} = \gamma\left[M_y(t)B_z - M_z(t)B_y\right] - \frac{M_x(t)}{T_2} \tag{1.28}$$

$$\frac{d\,M_y(t)}{dt} = \gamma\left[M_z(t)B_x - M_x(t)B_z\right] - \frac{M_y(t)}{T_2} \tag{1.29}$$

$$\frac{d\,M_z(t)}{dt} = \gamma\left[M_x(t)B_y - M_y(t)B_x\right] - \frac{M_z(t) - M_0}{T_1} \tag{1.30}$$

The solution to the Bloch equations [Eq 1.31] shows the following time dependence of the magnetization [1].

$$M_z(t) = M_z(0)e^{-\frac{t}{T_1}} + M_0\left(1 - e^{-\frac{t}{T_1}}\right) \quad 1.31$$

where M_0 is the magnetization at equilibrium, $M_z(t)$ is the longitudinal magnetization at time *t*, and $M_z(0)$ is the longitudinal magnetization at $t = 0$ (before perturbation). To simplify let's assume $M_z(0) = 0$, then the equation becomes:

$$M_z(t) = M_0\left(1 - e^{-\frac{t}{T_1}}\right) \quad 1.32$$

Following a perturbation, that tilts magnetization to *x,y* plane, the longitudinal magnetization $M_z(t)$ experiences exponential regrowth towards equilibrium and aligns with the $\vec{B}_0$ field. The T_1 relaxation time refers to the time it takes for the signal to grow $1 - e^{-1}$, 63% of its maximum value [6] due to exponential return (Fig. 3). Both relaxation times T_1 and T_2 vary for different tissues, providing tissue contrast in MRI.

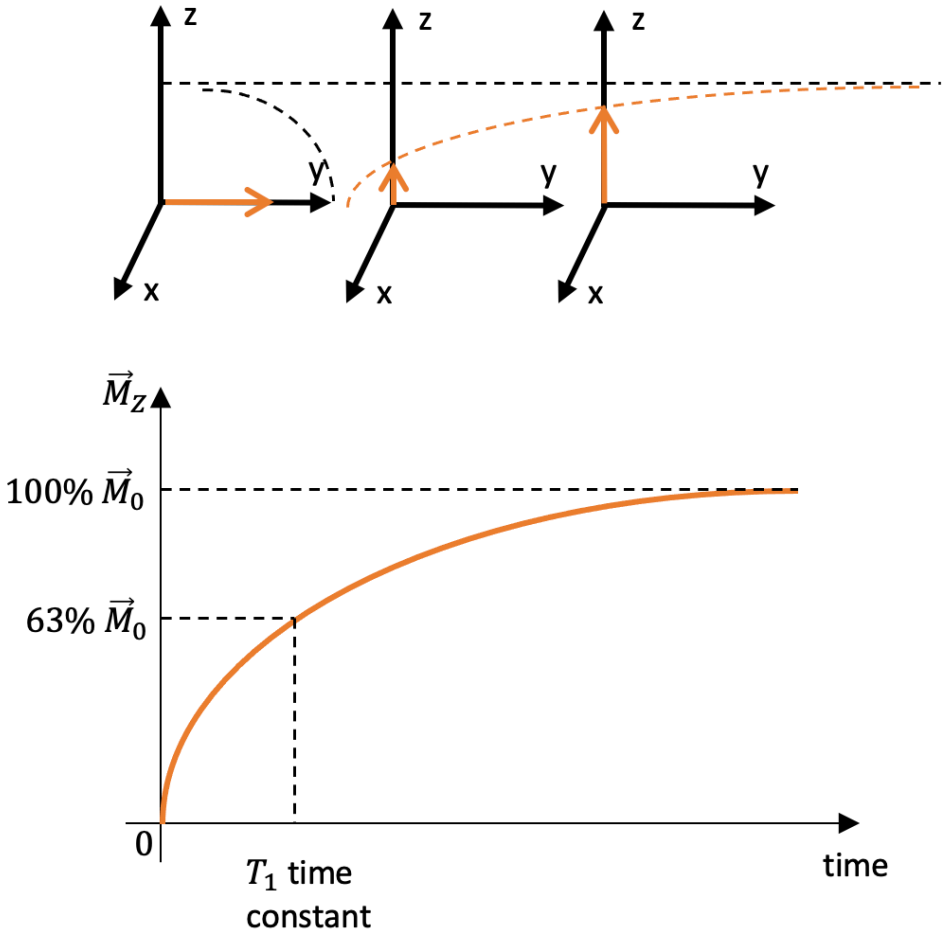

Fig. 3. *Return of the magnetization $\vec{M}_z$ following the application of a 90° RF pulse. The magnetization returns exponentially to its equilibrium with the relaxation time T_1.*

1.4.1 Radiofrequency Pulses and Free Induction Decay

When nuclear spins are perturbed from their equilibrium they begin precess around the external magnetic field $\vec{B}_0$. This perturbation is typically induced by an RF pulse, which can flip the spins to the transverse plane perpendicular to the $\vec{B}_0$, namely into the *x,y* plane. A pulse that rotates the spins by 90° is called a 90° pulse. The magnetisation, according to the Faraday's law, induces the electromagnetic force (EMF) in the receiving RF coil, called free induction decay (FID), which is a waveform that is subsequently digitalized using analog-to-digital converters (ADC) to produce the NMR signal. When the time-varying magnetic field gradients are applied, the same principle is used to construc the MR images, as explained in Chapter 2.

1.4.2 T_2 and T_2^* Relaxation

Transverse relaxation, or so-called spin-spin relaxation, describes the decay of the transverse component of magnetization ($\vec{M}_{xy}$ perpendicular to $\vec{B}_0$) back to zero. This process follows an exponential decay, as seen in the equation below:

$$\vec{M}_{xy}(t) = \vec{M}_{xy}(0)e^{-\frac{t}{T_2^*}} \tag{1.33}$$

where T_2^* is the transverse relaxation time. It is defined as the time for the signal to decrease $\frac{1}{e}$ of its original value (37%).

T_2^* relaxation refers to the decay of transverse magnetization caused by both spin-spin interactions and magnetic field inhomogeneities [7]. Due to these processes, the transverse magnetization decays over time, and the rate of this decay is denoted as the T_2^* relaxation time. The relationship between T_2^* and T_2 is:

$$\frac{1}{T_2^*} = \frac{1}{T_2} + \gamma \Delta B \tag{1.34}$$

where $\gamma\Delta B$ is the relaxation due to the field inhomogeneities within a sample [7] hence $T_2^* \leq T_2$ (Fig 4).

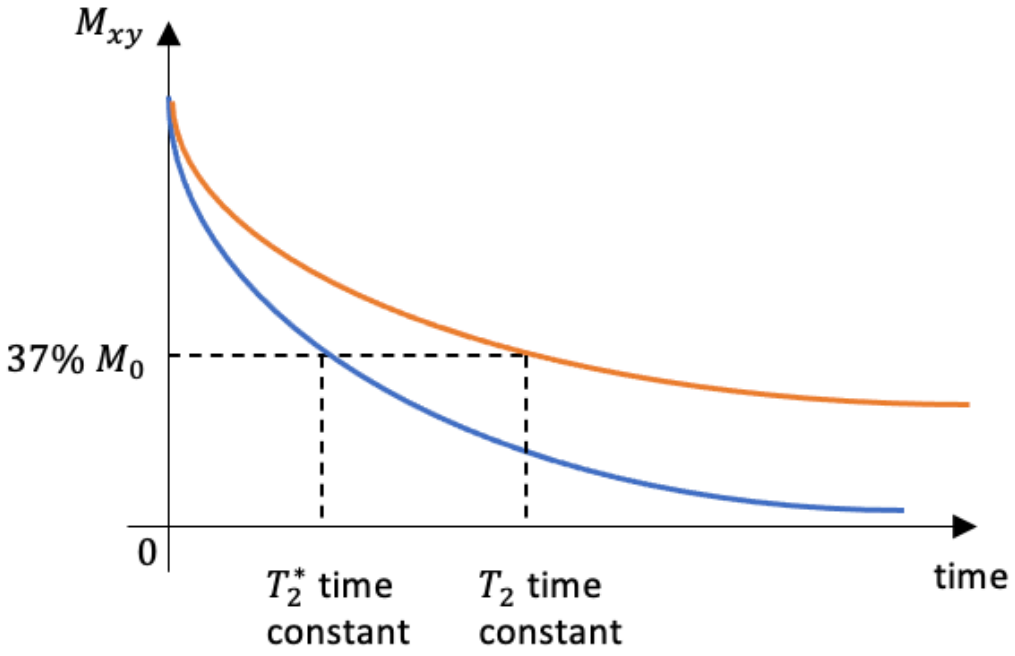

Fig. 4. *Decay of the transverse magnetization M_{xy} following a 90° RF pulse showing the relaxation time T_2 (orange line) and T_2* (blue line) in the presence of field inhomogeneities.*

1.4.3 Relaxation Rate and Relaxivity

Relaxation rates ($R_{1,2}$) and relaxivities ($r_{1,2}$) are frequently used terms to describe molecular dynamics, and potency of contrast agents in medical MR imaging. The $R_{1,2}$ is defined as:

$$R_{1,2} = \frac{1}{T_{1,2}} \, [s^{-1}] \tag{1.35}$$

while $r_{1,2}$:

$$r_{1,2} = \frac{1}{CT_{1,2}} \, [mM^{-1}s^{-1}] \tag{1.36}$$

where, C is concentration in millimoles (mM) of the nanoparticles in a solution hence provide information regarding efficacy of a contrast agent.

High relaxivity values of a contrast agent are desired as they provide strong relaxation shortening. Efficient contrast agents accumulate in tumors increasing tumor contrast in MRI with low concentration of potentially toxic nanoparticles. Nanoparticle relaxivity depends on a number of factors, such as chemical composition, magnetic properties, surface potential or size. These properties can be modified to obtain maximum changes in relaxation times hence optimal contrast in MRI with minimum concentrations of contrast agents and low toxicity, [8].

Table 1 summarizes selected properties of various contrast agents used in MRI, including their surface coatings, sizes, relaxivities and the magnetic field strengths at which they were measured. Among the compared agents, superparamagnetic iron oxide-based nanoparticles (e.g., Combidex, Feridex®, and Resovist) and lanthanide-based nanoparticles (e.g., $NaDyF_4$ and Dy-DTPA derivatives) are provided as they are related to the thesis. The high r_2 relaxivity of $NaDyF_4$ at 9.4T makes it a strong candidate for T_2-weighted imaging. This table indicates the significance of particle size, surface coatings, and magnetic field strength in determining the efficiency and applicability of MRI contrast agents.

Contrast Agent	Surface Coating	Size (nm)	r_1 $(mMs)^{-1}$	r_2 $(mMs)^{-1}$	Field (T)	Ref
$NaDyF_4$	PMAO-PEG	20.3	0.33	101	9.4	[9]
Dy-fullerenol				20	9.4	[10]
Dy-DTPA-$PcHexPh_2$			0.11	3	7	[11]
Dy_2O_3	D-glu. acid	2.9	0.16	40	3	[12]
Combidex (Fe_3O_4)	Dextran	5.85	10	60	1.5	[13]
Feridex (Fe_3O_4, γ- Fe_2O_4)	Dextran	4.96	4.1	93	3	[14]
Resovist (Fe_3O_4)	Carboxydextran	4	4.6	143	3	[14]
Fe_3O_4	H_2N	7.4	0.11	3.8	9.4	[Our results]

Fe_3O_4	H_2N	7.4	0.44	3.0	3	[Our results]

Table 1. *Comparison of MRI contrast agents, showing their surface coatings, sizes, relaxivities at various magnetic field strengths.*

Chapter 2. Major Components of a Magnetic Resonance Imaging System

MRI, unlike most other bioimaging modalities, does not utilize ionizing radiation which is associated with potential long-term health risks due to possible radiation induced cancer development. This non-ionizing nature of MRI makes it a safe alternative, particularly for repeated imaging sessions, and for vulnerable populations such as children and pregnant women. Moreover, MRI provides exceptional soft tissue contrast, enabling clear differentiation between various tissues, which is crucial for accurate diagnosis and treatment planning.

There are 3 major hardware components of an MRI system (Fig 5): magnet (consisting of superconductive wires placed within a cryostat), gradient coils and RF coils.

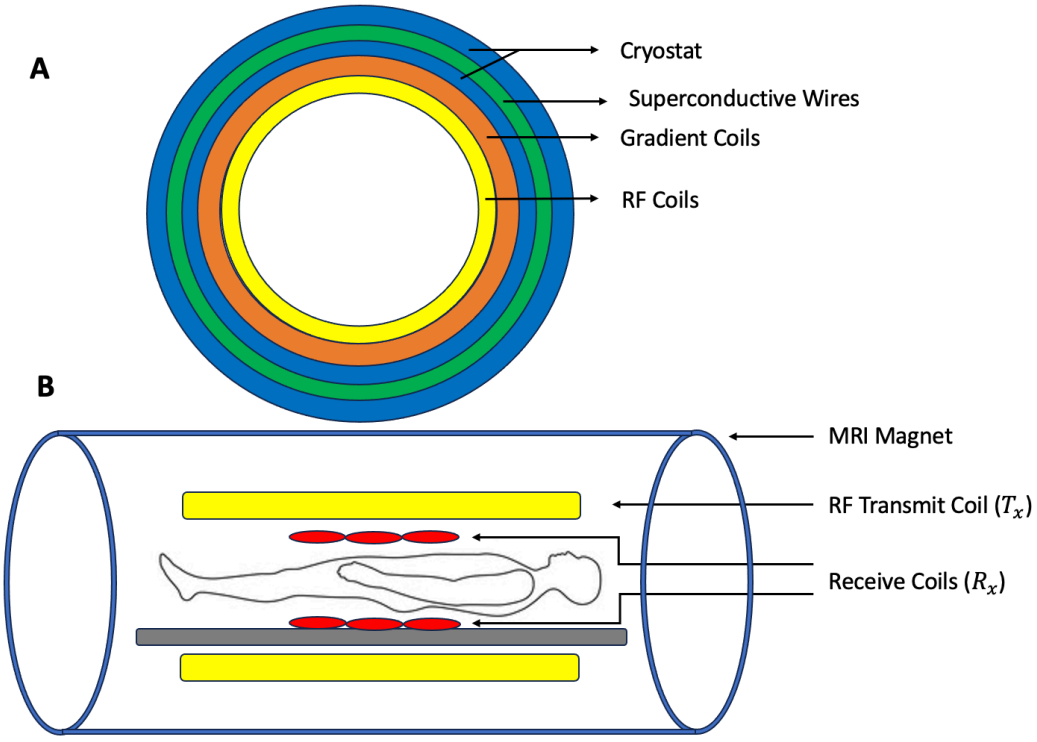

Fig. 5. *(A) Major hardware components of a clinical MRI system: magnet, gradient coils, and RF coils. The magnet comprises superconductive wires placed within the cryostat. Gradient coils are placed inside the bore of the magnet. Transmit RF coils are located inside the gradient coils, while the receive coils are in the proximity of the patient; (B) RF coils in an MRI scanner: Transmit (Tx) coil (yellow) and phase array receiving (Rx) coils (red).*

2.1 Magnet

To create a strong magnetic field various types of magnets are used: superconductive, permanent and electromagnets. Higher magnetic field strengths provide higher MR signal intensity (S) according to the equation [1]:

$$S \propto B_0^2 \qquad 2.0$$

Higher signal enables higher spatial resolution imaging per scan time allowing more detailed visualization of anatomical structures and pathological changes as compared to lower field magnets. Consequently, the use of high field MRI systems is particularly advantageous in clinical and research settings where detailed imaging is essential for accurate diagnosis and assessment.

Most clinical, MRI systems utilize superconductive magnets with a magnetic field strength of 1.5T and 3T, whereas pre-clinical systems used in animal experiments have stronger magnetic field strengths of 7T, 9.4T, 11.7T, 16T and even higher. Superconducting magnets are constructed from coils made of superconducting materials, that when cooled to cryogenic temperatures (using liquid helium), exhibit zero electrical resistance. This allows for the efficient generation of strong and stable magnetic fields. These magnets provide the highest special resolution and signal to noise ratios (SNR), making them ideal for detailed imaging and advanced diagnostic applications. However, they require complex cooling infrastructure and involve higher initial and maintenance costs compared to low field systems based on permanent magnets.

In contrast, permanent magnets produce a magnetic field strength to maximum of 0.35T. They are made of stacked magnetic alloys and do not require cryo-cooling components. While they are cost effective in terms of both acquisition and ongoing operation, they offer lower image resolution However, they can provide better contrast than high field systems for some tissues, such as white and grey matter, due to larger differences in relaxation times between these tissues as T_1 and T_2 depend on the field strength.

Another category is resistive magnets, which magnetic fields up to 0.5T. These magnets use electric current passing through conductive coils generating the magnetic field. The field strength can be adjusted by changing the current. Resistive magnets require a continuous and stable power supply as well as cooling system to dissipate heat generated by the electric current. As a result, resitive systems tend to have unstable magnetic fields, high energy consumption, and elevated operational costs, limiting their use in clinical settings.

2.1.1 Gradient System

The gradient system in MRI consists of three orthogonal gradient coils and their associated amplifiers. The coils generate time-varying magnetic fields that enable spatial signal encoding of the MR signal. Several parameters characterize performance of the gradient coils, including the maximum gradient strength (mT/m), rise time (s) and the gradient rate at which this maximum strength can be attained (mT/m/s). In clinical imaging systems, maximum gradient strength varies from approximately 30 to 45 mT/m [15]. This range reflects the balance between the need for stronger gradients to achieve better spatial resolution and the constraints imposed by safety considerations as the increased gradient strengths and rate produce loud noise and may even cause peripheral nerve stimulation [2].

The typical rise time of the gradient in MRI is between 0.1ms to 0.5ms [16]. However, in faster imaging methods, such as echo planar imaging (EPI), demanding rapid changes of gradient for fast data acquisition, rise time shorter than 0.1ms may be used [2]. This is necessary to reduce the total scan time hence to minimize motion artifacts albeit with costs of potential eddy currents induced in the magnet generating artifacts in MR images.

Higher gradient strengths are often required in diffusion MRI compared to conventional MRI, to accurately measure the diffusion coefficients of water molecules. In these specialized applications, gradient strengths from 15 to 300 mT/m are used. These high gradient strengths are essential for achieving the necessary spatial and temporal resolution to detect the subtle diffusion processes within the body [17].

2.1.2 RF Coils

Radiofrequency (RF) coils are used to transmit the RF pulses exciting spins in the sample as well as to receive the relaxation signals emitted by the protons following the RF pulse [2]. The RF coils may be transmit-only, receive only or both. They resonate at RF, corresponding to the Larmour frequency. In clinical systems, the transmit RF coil is placed close to the gradient coils, within the bore of the magnet, to ensure homogenous spin excitation, while the receive coils are placed close to the patient to increase coils sensitivity hence provide high image quality, as seen in Figure 5B.

In most pre-clinical MRI systems, a single coil serves as both the transmit and receive coil. These integrated coils are known as transmit/receive RF coils. In pre-clinical applications, when high imaging resolution is required, the coil is often submersed in liquid helium reducing thermal noise hence the coil resistance leading to improved SNR

The electromagnetic force (EMF) induced by the nuclear magnetization in the receiving coil follows the equation [18]:

$$\Psi_{rms} = K\eta \mathrm{M}_0 \left(\frac{\mu_0 Q \omega_0 \mathrm{V}_c}{4Fk\mathrm{T}_c\Delta \mathrm{f}}\right)^{\frac{1}{2}} \qquad 2.1$$

where: Ψ_{rms} is the root mean square (rms) value of the NMR signal or the induced EMF in the receiving coil, $K$is a numerical factor that depends on the coil geometry, η is the filling factor, which represents the fraction of the RF field volume occupied by the sample, Q is the quality factor of the coil, representing how efficiently it stores energy, V_c is the volume of the coil, F is the noise figure of the preamplifier, T_c is the temperature of the coil and Δf is the bandwidth of the receiver. Reciprocity theory developed by Hoult [18] assumes that the efficiency of an RF coil in transmitting an RF field and in receiving a signal is the same, hence the equation 2.1 evolves to:

$$\Psi_{rms} = \frac{K(B_1)_{xy} V_s N \gamma \lambda^{\,2} I(I+1)}{7.12kT_s} \cdot \left(\frac{p}{FkT_c l \zeta \Delta f}\right)^{\frac{1}{2}} \cdot \frac{\omega_0^{\frac{7}{4}}}{\left(\mu\mu_0\rho(T_c)\right)^{\frac{1}{4}}} \qquad 2.2$$

where $K(B_1)_{xy}$ is the effective field over the sample volume produced by unit current flowing in the receiving coil, p is the perimeter of the conductor, l is the length of the conductor, $\rho(T_c)$ is the resistivity of the material from which the coil is made, and ζ is the proximity factor.

The relationship between SNR and the coil temperature, bandwidth and resistance is described by the following equation [1]:

$$SNR = \frac{\Delta M_{\perp} B_{\perp}}{\sqrt{4kT_c \Delta f R_{eff}}} \qquad 2.3$$

where $M_{\perp}$and $B_{\perp}$ are transverse components of the magnetization and magnetic field respectively, R_{eff} is the effective resistance of the coil. As seen from the above equation SNR can be increased by cooling the coil, hence the application of cryo-coils in high field as high resolution MRI is required in small animal MRI.

2.2 Fourier Transform

In XVII century French mathematician Jean-Baptiste Joseph Fourier, introduced a formula allowing conversion of a time-domain function into a frequency-domain, that later became known as the Fourier Transform (FT). This technique was introduced to NMR by Richard R. Ernst in 1966 [19]. Ernst's contributions to the field were so impactful that he was awarded the Nobel Prize in Chemistry in 1991 for his work in the development of high-resolution NMR spectroscopy [20]. Later on, the FT was applied to MRI as it is crucial in the creation of an MR image because it converts time-domain information contained in the MR signal into frequency that in turn can be resolved into spatial domain, namely an MR image [20].

The FT of a continuous function f(t) is:

$$F(\omega) = \int_{-\infty}^{\infty} f(t) e^{-i\omega t} dt \qquad 2.4$$

where F(ω) is the Fourier transform of f(t), ω is the frequency, and $i = \sqrt{-1}$.

2.3 Image Creation (k-space)

The 2D k-space concept was introduced to explain and simplify image creation in MRI. Each line in k-space corresponds to a specific gradient configuration and is collected sequentially during the MRI scan (Fig. 6). Once the entire k-space is collected an inverse FT is applied to obtain an image. The traversing k-space process begins at the k-space centre (point A), then the phase encoding (k_{phase}) and frequency encoding (k_{freq}) gradients are applied (from point A to B). The frequency encoding gradient is applied during signal acquisition (B-C). The phase encoding gradient is varied in small steps between each repetition, causing the data to fill different lines of k-space. This process is repeated until all lines of k-space are collected, with each gradient configuration mapping to a unique line in k-space.

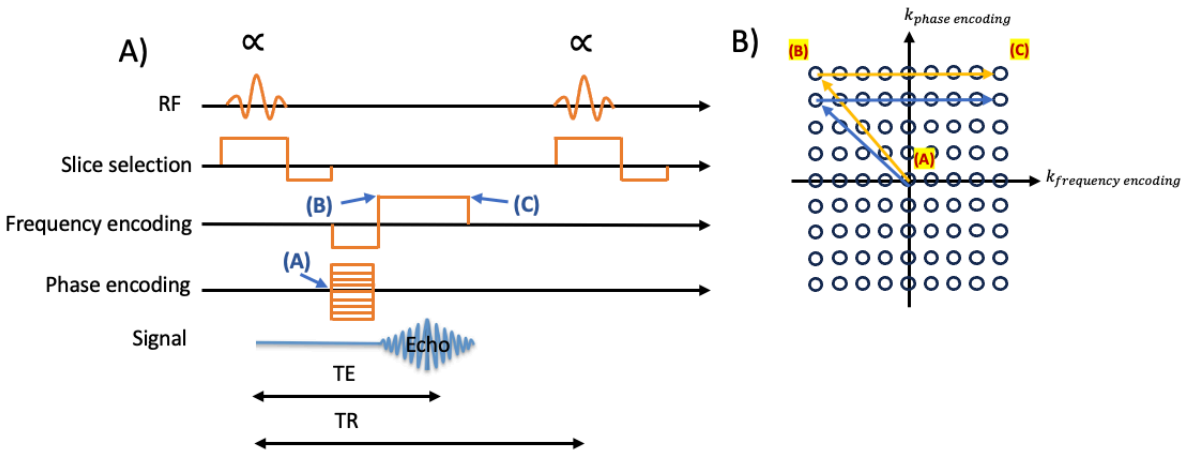

Fig. 6. *A) Gradient echo (GE) pulse sequence diagram; B) the corresponding traversal of k-space. Following the exitation pulse (k-space center) the phase and frequency encoding gradients are applied corresponding to the movement of the vector $\vec{k}$ to point B (yellow arrow). The polarity of the frequency encoding gradient is then reversed, causing $\vec{k}$ to traverse a horizontal line, resulting in the acquisition of the first phase encoding line until the frequency encoding gradient is complete at point C. The sequence is then repeated with a reduced amplitude of the phase encoding gradient to fill a new line. This process continues until the entire k-space is covered [21].*

The spatial dependence of the spin states within a sample is dependent on the gradients. These gradients cause the magnetic ($\vec{B}(\vec{r})$) field to vary linearly with position ($\vec{r}$) and are in the same direction as $\vec{B}_0$:

$$\vec{B}(\vec{r}) = \left(B_0 + \vec{r} \cdot \vec{G}_r\right)\hat{k} = \left(B_0 + \left\{xG_x + yG_y + zG_z\right\}\right)\hat{k} \quad 2.5$$

where $\vec{G}_r = \left\{xG_x + yG_y + zG_z\right\}\hat{k}$ is the field gradient (mT/m) in direction $\vec{r}$. The gradient fields cause spatially dependent magnetization phase to accumulate $\varphi(\vec{r}, t)$:

$$\varphi(\vec{r}, t) = \gamma\vec{r} \cdot \int_{t_0}^{t} \vec{G}_r(t')dt' \quad 2.6$$

While vector $\vec{k}$ is defined as:

$$\vec{k}(t) = \frac{\gamma}{2\pi}\int_{t_0}^{t} \vec{G}_r(t')dt' \quad 2.7$$

Hence the NMR signal using spatial frequency ($\vec{k}$) can be expressed as:

$$s(t) = \int_V \rho\,(\vec{r})e^{-i2\pi\vec{k}\cdot\vec{r}}\,d\vec{r} \quad 2.8$$

The signals emitted by protons in body's tissues are encoded through phase and frequency encoding techniques and stored as data points in k-space. The centre of k-space contains low spatial frequencies because lower gradient strengths capture broad structures and contrast. The edges hold high spatial frequencies since higher gradients capture fine details and sharp edges as seen in the Figure 7 below:

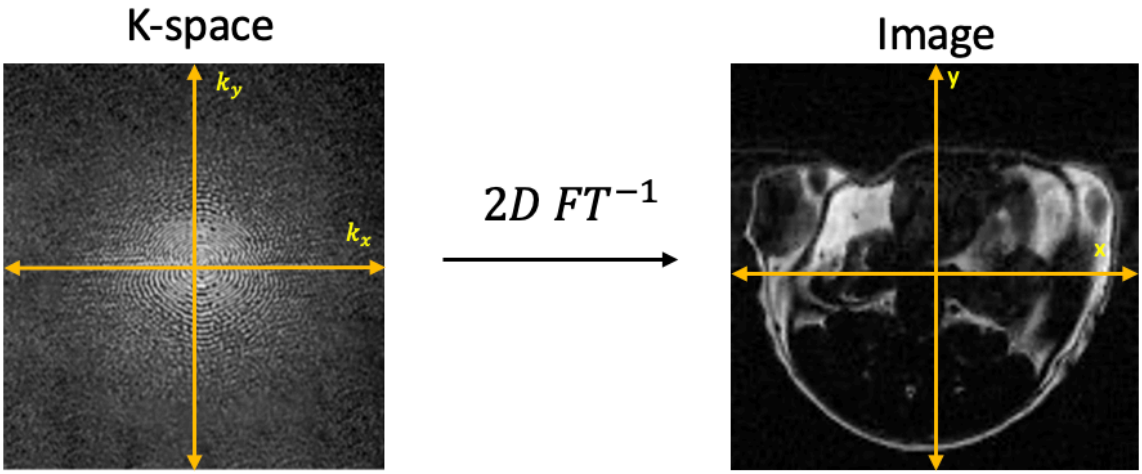

Fig. 7. *K-space and its Fourier transform: an MR image. The lines in the k-space represent data points collected in each phase encoding step (k_y).*

A 2D inverse FT is applied to convert the k-space data into the spatial domain, resulting in an image.

2.3.1 Slice Selection

The slice selection is accomplished in MRI by simultaneous application of a gradient and a frequency selective RF pulse. The FT of a perfect selective RF pulse has a rectangular profile.

The RF pulse bandwidth defines the slice thickness. Wider bandwidth (shorter RF pulses) excites a broader range of frequencies, resulting in a thicker slice, while narrower bandwidth (longer) pulses select a thinner slice. Precise control of RF pulse length (hence the bandwidth) is needed for optimizing image quality and diagnostic accuracy. The simplest and most frequently used pulse for slice selection is a sinc-shape $\left(\frac{\sin(x)}{x}\right)$ pulse, which FT is very close to the rectangular shape (Fig. 8).

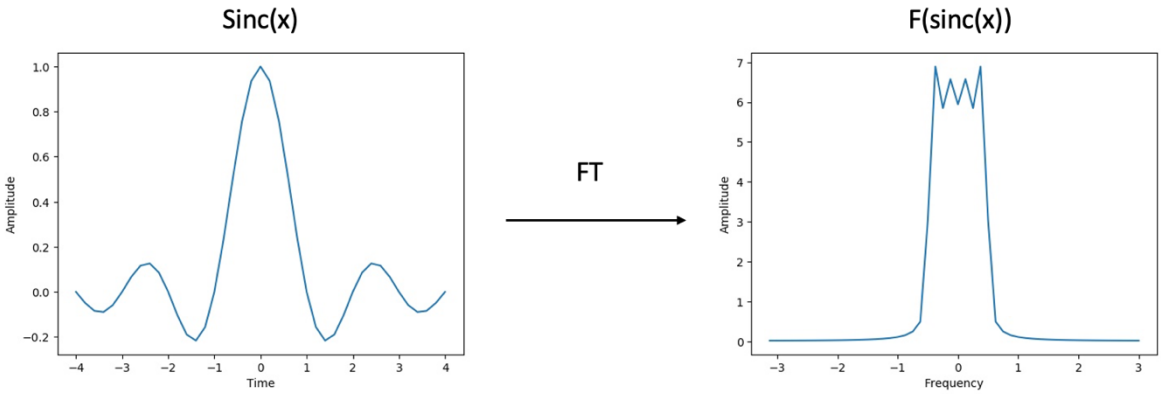

Fig. 8. *Sinc(x) function and its corresponding Fourier Transform.*

In the presence of a gradient along z direction the Larmour frequency changes as follows [22]:

$$\omega(z) = \omega_0 + \gamma G_z \qquad 2.9$$

The spins within the imaged slice have a specific Larmour frequency range due to the gradient field applied along the *z*-axis. When the RF pulse bandwidth corresponds to this range, a particular slice is selected. By changing RF pulse frequency individual slices may be selected (Fig. 9).

The thickness of a slice (Δz) is determined by the strength of the gradient and the bandwidth of the RF pulses. By using a stronger gradient or a narrower RF pulse bandwidth (longer pulse) the slice thickness is reduced, according to:

$$\Delta z = \frac{2\,\pi\,(RF\ Bandwidth)}{\gamma G_z} \qquad 2.10$$

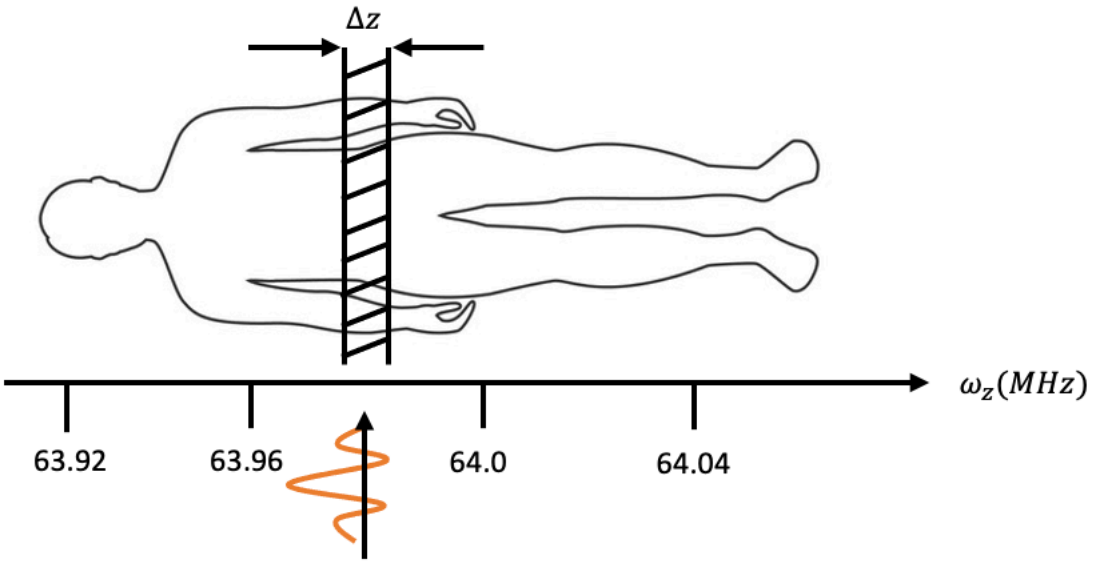

Fig. 9. *An example of slice selection using a gradient of the magnetic field at 1.5T. The selective RF pulse excites a slice Δz.*

2.3.2 MR Imaging

The MR signal S(t) from the sample of volume V in the presence of gradients can be expressed as [1]:

$$S(t) = \int_V \rho\,(\vec{r}) e^{-i\gamma \int_0^t \vec{G}(t')dt' \cdot \vec{r}}\, d\vec{r} \qquad 2.11$$

where $\rho(\vec{r})$ is the spin density distribution, $\vec{G}(t')$ is the time dependent gradient, V is the sample volume.

To produce an MR image, spins must be spatially localized. The spatial information is attained by superimposing time variable magnetic field gradients onto the main magnetic field. The inverse FT (FT^{-1}) relates the signal and the spatial distribution of spins (an image) as follows:

$$I(x,y) = FT^{-1}\{S(k_x, k_y)\} \qquad 2.12$$

where I(x,y) is the spatial distribution of spins, $S(k_x,k_y)$ is the spatial frequency domain signal [1].

2.4 Pulse Sequences

Pulse sequences in MRI refer to the series of RF pulses and gradients of the magnetic field applied to produce an image. The manipulation of pulse parameters provides image weighing, such as T_1-, T_2- or proton density-weighted that utilizes differences in relaxation times hence contrast. For example, T_1-weighted images provide good contrast between bones (appearing white) and fluid-filled areas (appearing black) due to short T_1 of bones and long of fluid; T_2-weighted images provide bright fluid-filled areas (long T_2) and protein content dark (short T_2). Proton density-weighted images are obtained using a pulse sequence that does not emphasize either T_1 or T_2 but provides an overall representation of the proton density of the tissue.

The most common pulse sequences are based on spin echo (SE) and gradient echo (GE) phenomena. Their T_1-weighting may be modified by proceeding the pulse sequence with a 180° inversion recovery (IR) pulse [23].

2.4.1 Spin Echo Pulse Sequence

The SE pulse sequence is based on the spin echo phenomena discovered by Hahn in 1950 can be seen in figure 10 below [24].

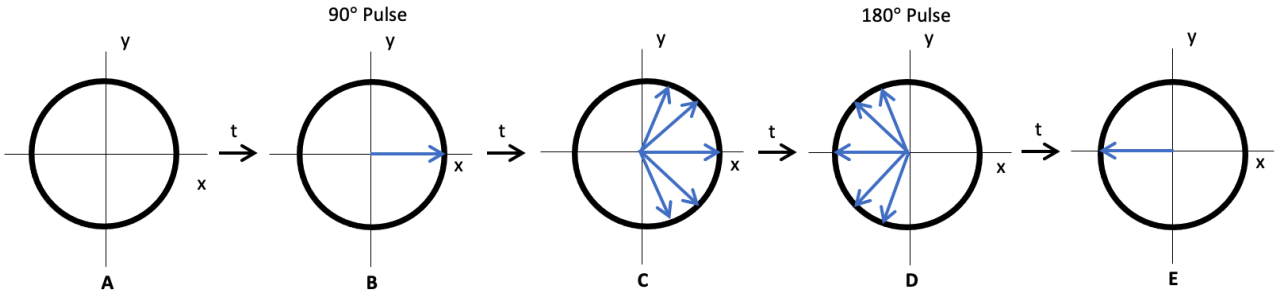

Fig. 10. *Formation of the spin echo after application of 90° and 180° pulses. Note: the echo is created at the same time t as the time distance between 90° and 180° pulse.*

To explain a spin echo formation, let's consider two RF pulses: a 90° and 180° (Fig. 10). The 90° RF pulse flips the spins into the transverse (*xy*) plane (Fig. 10B). The magnetization $\vec{M}(t)$ returns to its equilibrium due to the free induction decay (FID) and spins are dephasing (Fig. 10C). Then, after time TE/2 a 180° RF pulse is applied (Fig. 10D) causing spins flip around *y* axis hence to rephrase in the transverse plane. After TE the signal can be collected in the form of the echo (Fig 10E).

2.4.2 Slice Selective Spin Echo Imaging Pulse Sequence

The SE sequence begins with the application of a slice selection gradient, typically along the *z*-axis, during the selective RF pulse to excite spins within an imaging slice. Following the slice selection, the phase encoding gradient is applied along the *y* axis to encode spatial information in the *y*-direction. This gradient introduces a phase shift of the spins based on their position along the *y* axis. The phase encoding gradient is varied incrementally with each repetition of the sequence to capture data for different spatial locations, which will later be used to reconstruct the image. Finally, the frequency encoding gradient (or readout gradient) is applied along the *x* axis during signal acquisition. This gradient causes spins at different locations along the *x* axis to precess at different frequencies, allowing the MRI system to distinguish between signals originating from different positions along this axis. The combination of these gradients with the refocusing pulse results in a 2D spatially resolved image. A diagram of a spin echo (SE) pulse sequence can be seen in Figure 11 below.

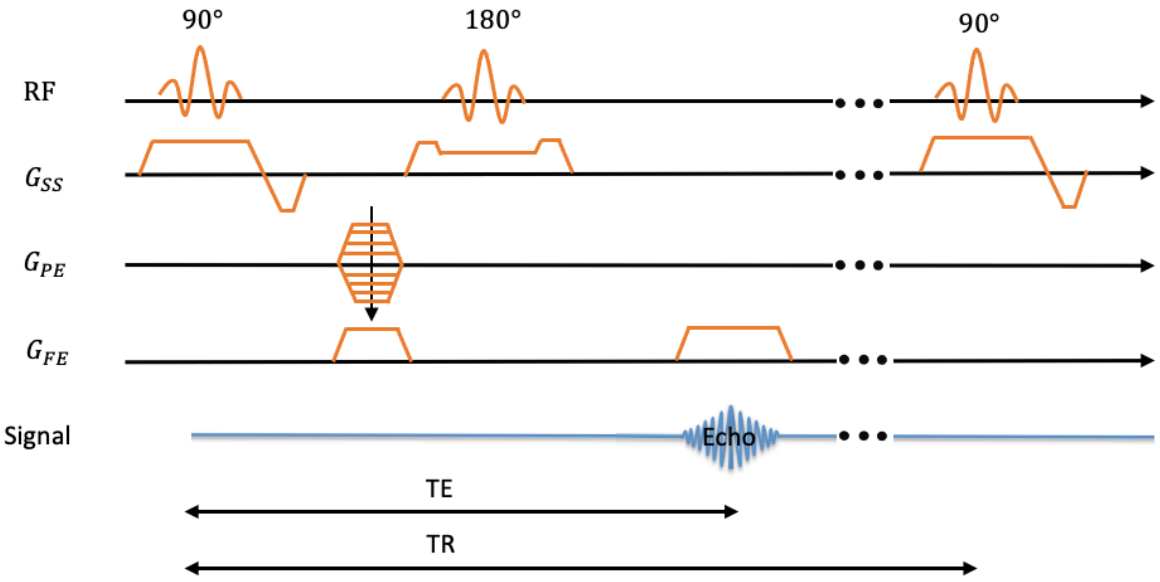

Fig. 11. *A spin echo pulse sequence. A 90° RF pulse is applied with a slice selection gradient. It is followed by a 180° RF pulse to refocus the spins at the echo time (TE). The phase encoding gradient encodes spatial information and changes incrementally over repeated cycles of the pulse sequence (after each repetition time (TR)). The frequency encoding gradient is applied during signal (echo) acquisition.*

Two parameters of the SE pulse sequence, repetition time (TR) and echo time (TE) vary depending on the desired image weighting and total scan time. The TE is defined as the time between the 90° RF pulse and the peak of the echo. The TR is defined as the time between the consecutive 90° RF pulses. Varying TR can provide T_1-weighing while varying TE can provide T_2-weighing. Due to differences in T_1 and T_2 relaxation times of various tissues, properly selected TR and TE can highlight specific tissues. This is the major advantage of MRI as a diagnostic tool [23].

2.4.3 Multi Slice Pulse Sequence

The SE slice selective pulse sequence can be extended to multi slice (MS) imaging (Fig. 12). In MS imaging, slice section is repeated for each slice, with slight variations of the frequency of the RF pulse to excite spins within selected slices (along the *z*-axis (Fig. 12). A 2D image is obtained for each slice as described in the above section.

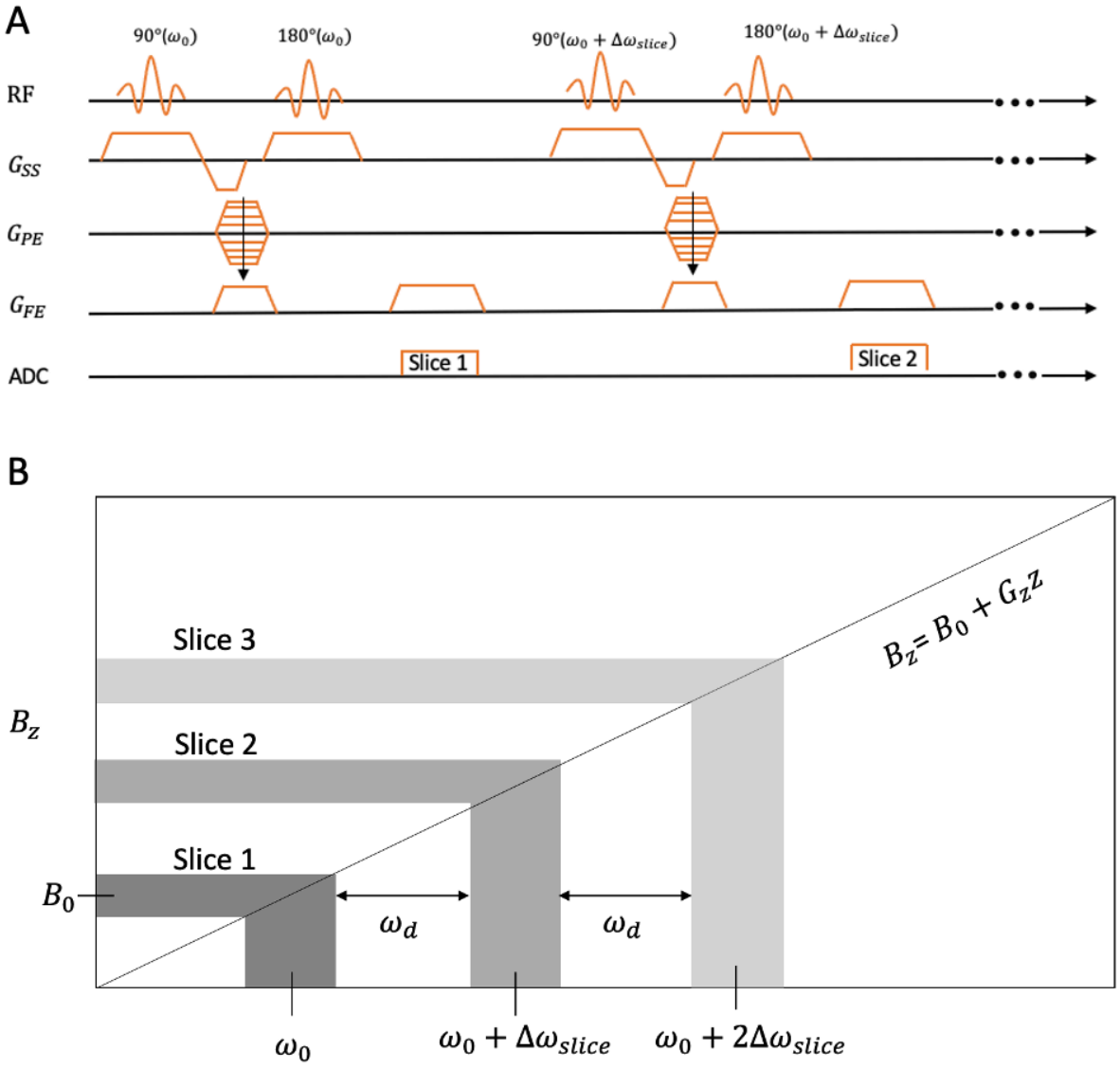

Fig. 12. *A multi-slice spin echo pulse sequence. Slices are imaged within TR time by the application of RF pulses with different frequency.*

2.4.4 Multi Echo Pulse Sequence

The multi echo (ME) pulse sequence allows acquisition of multiple spin echoes, each with different TE enabling different T_2-weighting of each image. This is accomplished by applying successive 180° pulses, each producing a new echo with different TE (Fig. 13). The images are collected from each echo as described above. Figure 13 shows the timing of these pulses (gradients are omitted) for multiple echo creation. This series of echoes provides a set

of images that can be used to calculate T_2 relaxation times using exponential fitting of the signal intensity in each image on pixel by pixel basis. Figure 13 shows also free induction decay (FID) with T_2* (see Eq 1.34 for reference).

T_2-weighted images are used to detect abnormalities in tissues such as edema, inflammation, cancer or fluid-filled spaces. T_2- maps show T_2 values of each pixel [23].

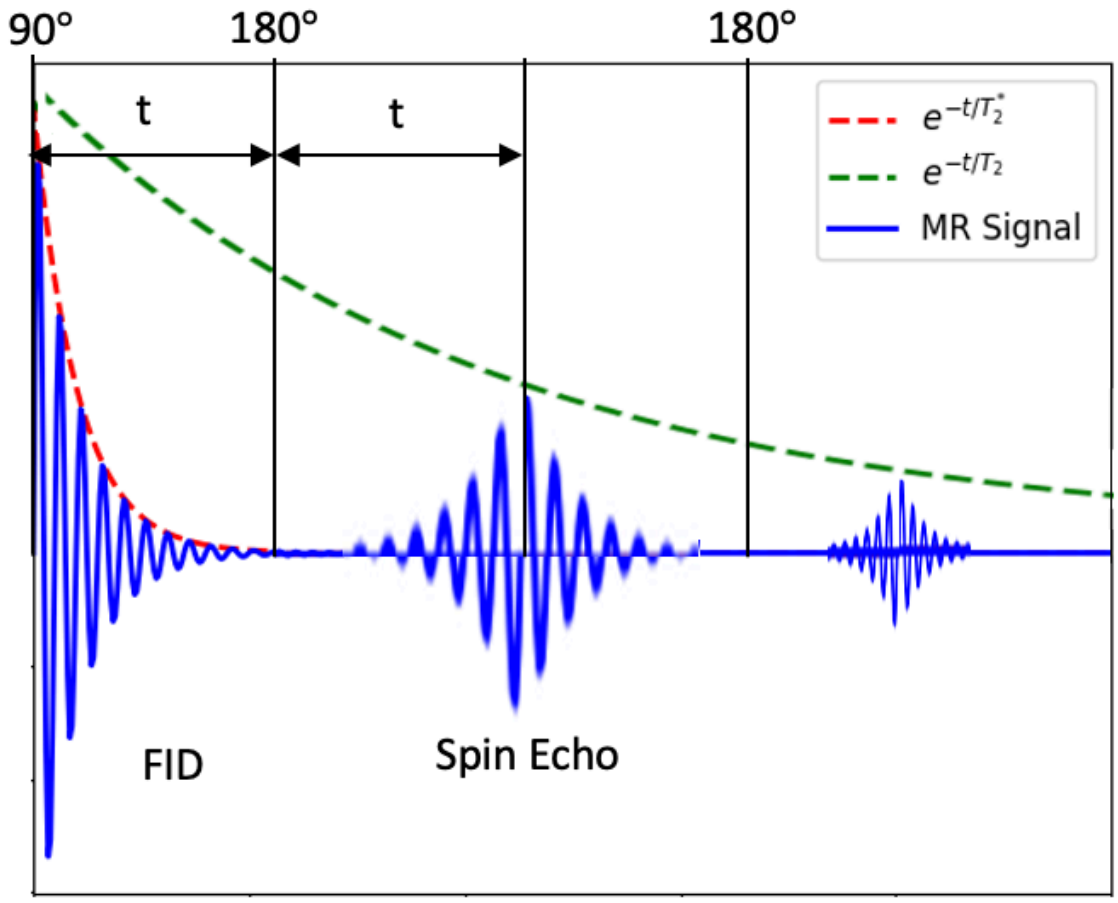

Fig. 13. *A multi-echo (ME) generation showing T_2 and T_2^* relaxation times. The sequence allows T_2 quantification using monoexponential fitting. FID is also shown for reference.*

2.4.5 Rapid Acquisition with Relaxed Enhancement Pulse Sequence

The Rapid Acquisition with Relaxation Enhancement (RARE) pulse sequence is a fast MRI imaging technique developed to improve imaging efficiency and contrast by acquiring

multiple echoes with proper phase encoding reversal within a single TR (Fig. 14). RARE significantly reduces scan times while enhancing SNR especially for tissues with long T_2 relaxation times, making it highly effective in detecting lesions with long T_2 values, such as those in neurological imaging [25].

Both RARE and multi-echo spin-echo (MESE) sequences generate multiple echoes following a single RF excitation pulse, but they differ significantly in how they use these echoes. The RARE sequence uses multiple echoes within TR to acquire a single image. This approach contrasts with the MESE sequence, where multiple echoes are used to obtain images at various TE from a single excitation, typically for T_2 mapping rather than for fast imaging. In MESE, the echoes are used to quantify T_2 values without accelerating the imaging time while RARE provides fast imaging [25].

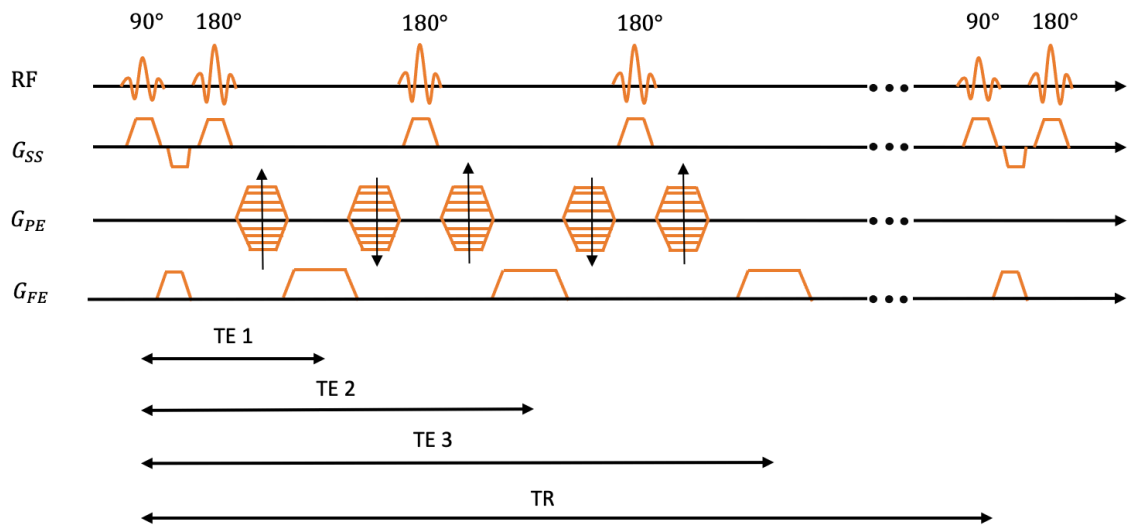

Fig. 14. *The Rapid Acquisition with Relaxation Enhancement (RARE) MRI pulse sequence diagram. Phase encoding gradients are rewound between each echo to collect points in k-space with one excitation reducing acquisition time. The slice selection and frequency encoding are performed as in SE pulse sequence. The image is weighted with the T_2 relaxation time.*

2.4.6 Inversion Recovery Pulse Sequence

The inversion recovery (IR) pulse sequence allows T_1-weighted imaging. It involves magnetisation inversion, recovery and signal acquisition. For the inversion, a 180° RF pulse is applied followed by an IR time when the 90° pulse is applied. The length of the recovery time determines the T_1 contrast. Subsequent, a 90° pulse followed by a 180° pulse are applied along with slice, phase and frequency encoding gradient to collect an MR image (Figures 15 and 16).

By adjusting the IR time, it is possible to create images with high T_1 contrast between different types of tissues, such as fat and fluids. In particular, the IR pulse sequence can be used to create images minimizing signal from fluids - fluid-attenuated inversion recovery (FLAIR) images. In this case, TR is set to null signal from fluid when the 90° pulse is applied. FLAIR images are used to visualize the anatomy of the body by suppressing the signal from cerebrospinal fluid (CSF) in the brain allowing detection of certain types of lesions or tumors [23].

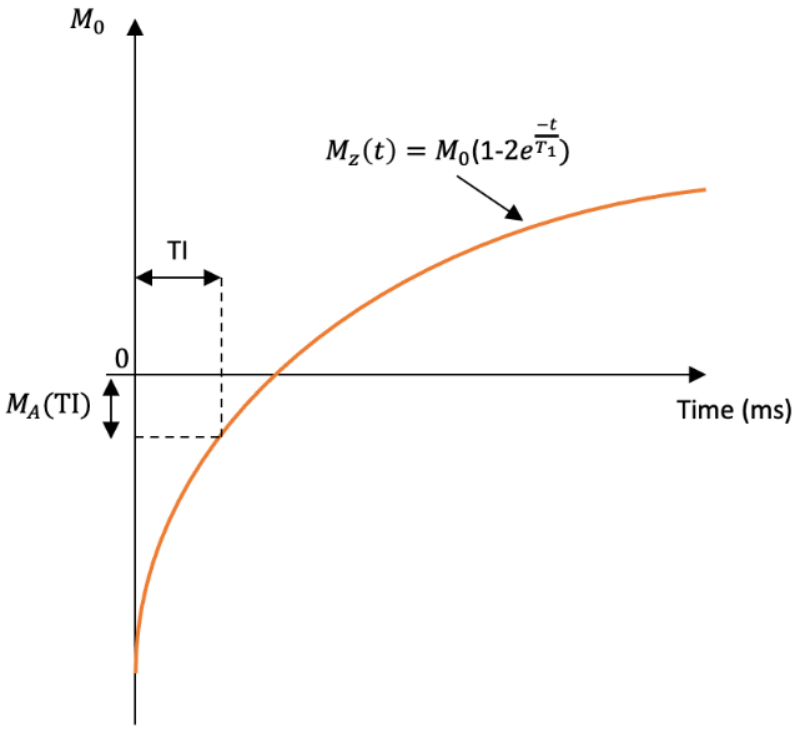

Fig. 15. *The graph shows the recovery of the longitudinal magnetization M_z as a function of time following the inversion pulse. A pulse sequence (e.g SE) is applied at time TI.*

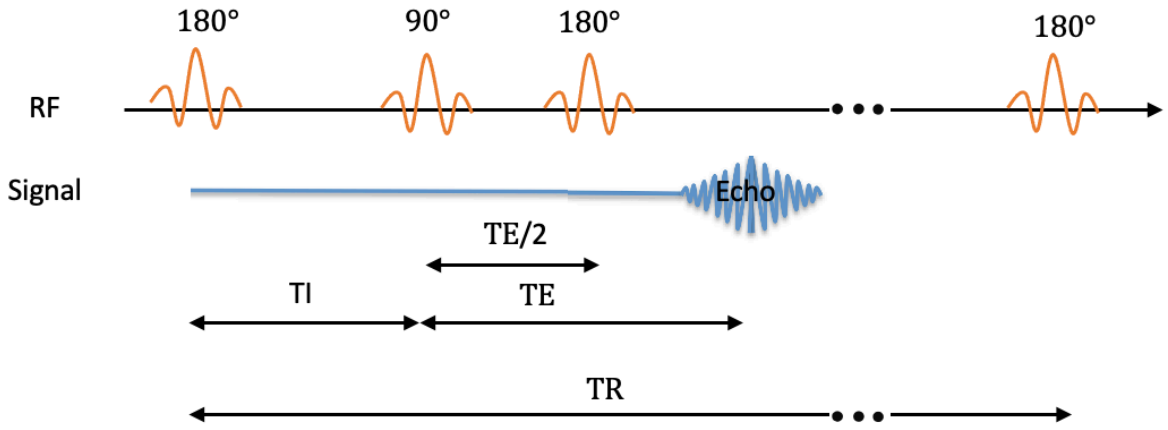

Fig. 16. *Inversion Recovery Spin Echo (IRSE) pulse sequence: a 180° inversion pulse inverts the longitudinal magnetization and is followed by SE pulse sequence. During inversion recovery time (TI) the magnetisation returns to equilibrium with T_1 relaxation time providing T_1 weighting that depends on TI. (Gradient wave forms are omitted for clarity).*

2.4.7 Gradient Echo Pulse Sequence

In a gradient echo (GE) pulse sequence (Fig. 17), a reverse frequency encoding gradient is used to generate the echo, hence the name: gradient echo. It is followed by phase and frequency encoding gradients as in the SE pulse sequence.

The GE sequence is faster than SE sequences as it does not require 90° and 180° pulses. It uses only one RF pulse, usually with small flip angle, enabling fast data collection. GE provides T_2^*-weighted images unlike SE, due to lack of the refocusing 180° pulse eliminating field inhomogeneities. This results in faster signal decay T_2^* compared to T_2, due to the uncorrected dephasing caused by the field inhomogeneities [Eq 1.34]. As such, susceptibility effects, caused by for example by contrast agents, and inhomogeneities of the magnetic field are prominent [16].

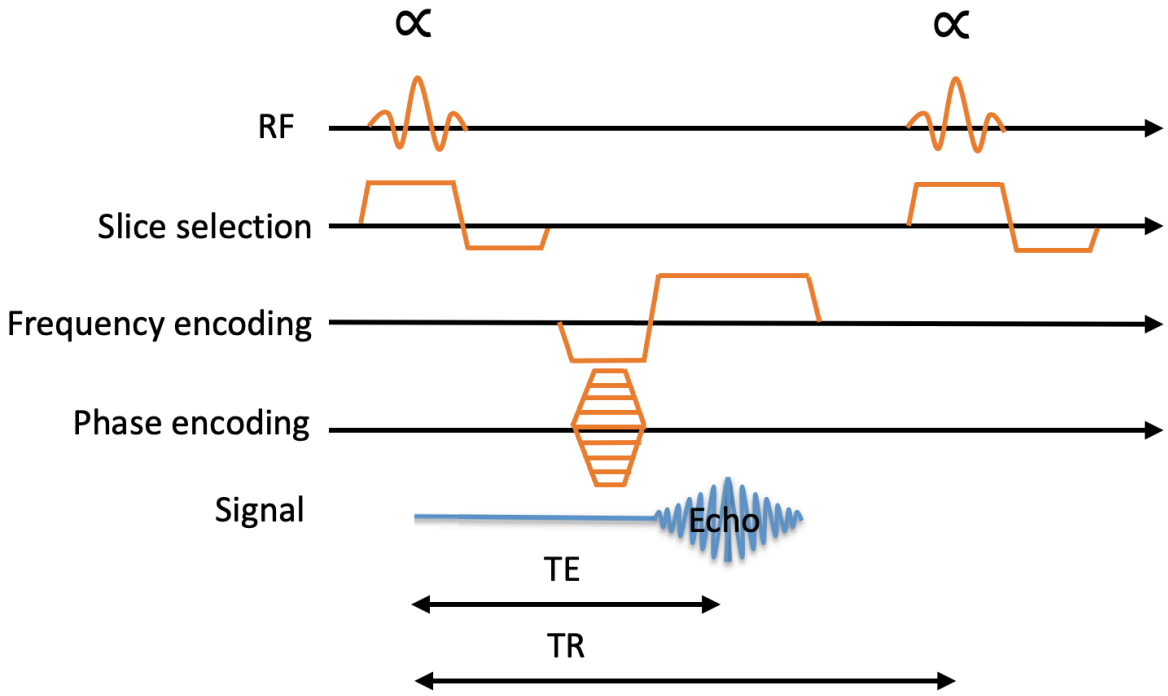

Fig. 17. *The gradient echo (GE) pulse sequence. The echo is created by the reverse frequency encoding gradient enabling application of small flip angle allowing fast imaging.*

2.4.8 Fast Imaging with Steady-State Precession Pulse Sequence

The Fast Imaging with Steady-state Precession (FISP) pulse sequence [26] is a rapid GE (short TE) MRI technique that uses gradient echoes produced by low flip angle RF pulses (~15°). Fast repeated RF pulses produce magnetisation equilibrium state. The spins phase is rewound by applying opposite phase encoding gradient before the next RF pulse. This allows residual transverse magnetization to persist across RF excitations, thus preserving signal [26]. Phase and read gradients are used in the same fashion as in standard SE imaging [26]. This balanced state of the transverse magnetization leads to mixed T_1 and T_2 contrast in the images. The precise weighting depends on the chosen TR, TE and flip angle, with longer T_2 tissues often appearing bright due to reduced dephasing. Consequently, the FISP sequence is versatile for clinical applications where high-resolution imaging is necessary within a short scan time [26]. An example of the FISP pulse sequence can be seen in Figure 18 below.

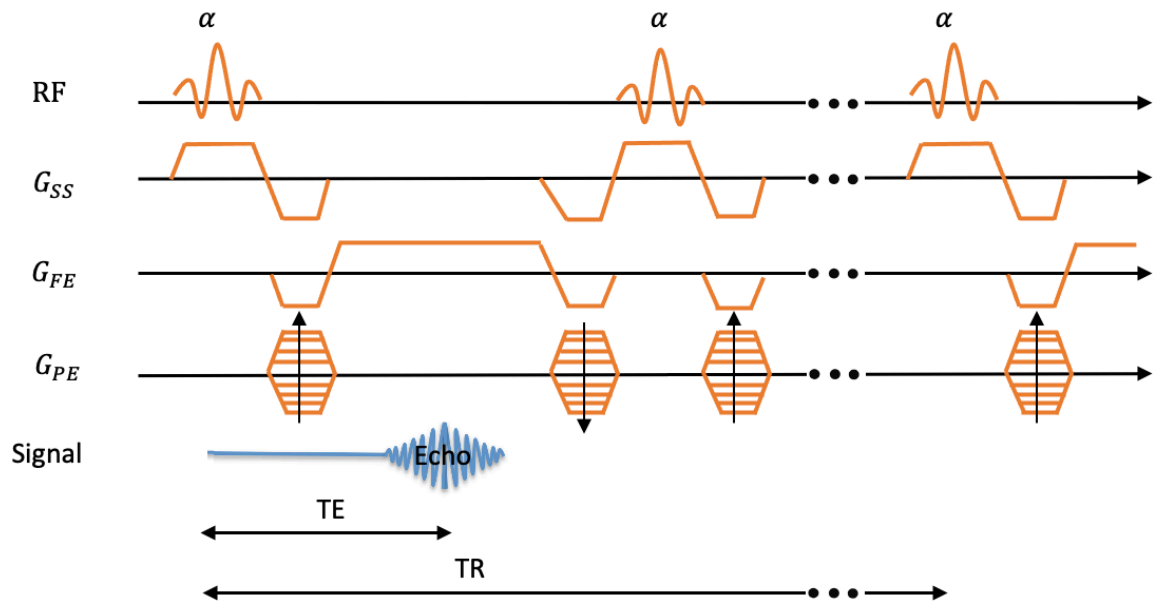

Fig. 18. *A Fast Imaging with Steady-state Precession (FISP) pulse sequence. The small angle pulses are used and are applied at regular short intervals to maintain a steady-state transverse magnetization. The slice selection, phase and read gradients are used as in a standard GE imaging. The FISP sequence allows a rapid acquisition of T_1/T_2-weighted images by maintaining coherent transverse magnetization [26].*

2.4.9 Inversion Recovery Fast Imaging with Steady-State Precession Pulse Sequence

The Inversion Recovery Fast Imaging with Steady-State Precession (IR-FISP) sequence is a modification of the conventional FISP technique that incorporates an initial inversion pulse to enhance tissue T_1 contrast. The sequence begins with a 180° inversion pulse, followed by a variable TI and a rapid FISP acquisition train. This combination allows for simultaneous exploitation of T_1-weighted contrast and T_2/T_2^* dependent steady-state signal behavior.

IR-FISP is particularly useful in small animal imaging and tumor detection, where it enhances sensitivity to tissue-specific relaxation differences while maintaining a fast acquisition time. The flip angle, TI, TE and TR parameters can be adjusted to modulate contrast characteristics depending on the imaging goal. Compared to standard FISP, the addition of the inversion pulse in IR-FISP suppresses specific tissues (e.g., fat or muscle) and improves

contrast-to-noise ratio for target structures such as tumors. An example of the IR-FISP pulse sequence is illustrated in Figure 19, showing the inversion pulse followed by the FISP readout scheme [26].

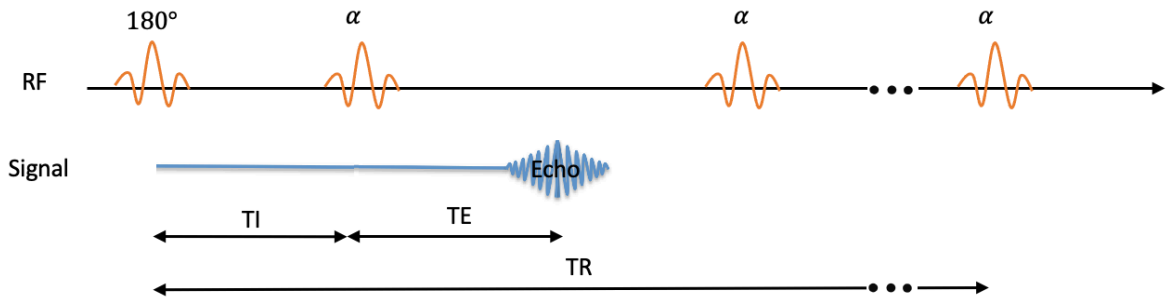

Fig. 19. *Inversion recovery fast imaging with steady state precession: a 180° inversion pulse that inverts the longitudinal magnetization is followed by FISP. (Gradient wave forms omitted for clarity).*

2.5 Signal Intensity and Pulse Sequence Parameters

2.5.1 Signal Intensity in SE Imaging

The signal amplitude in an MR image depends on both relaxation times and the applied pulse sequence parameters. For example, in SE T_1-weighted image, when TE is short, signal can be expressed as [1]:

$$S \propto \left(1 - e^{\frac{-TR}{T_1}}\right) \qquad 2.13$$

where S is the NMR signal amplitude, T_1 is the relaxation time, TR is the repetition time. A shorter T_1 relaxation time provides a higher signal intensity for the same TR.

In a T_2-weighted imaging (TE long, TR long) the NMR signal S can be expressed as [1]:

$$S \propto e^{\frac{-TE}{T_2}} \qquad 2.14$$

where S is the NMR signal intensity, T_2 is the relaxation time and TE is the echo time. Tissues with longer T_2 values retain their signal longer, appearing brighter, whereas tissues with shorter T_2 values exhibit faster signal decay and appear darker on T_2-weighted images. Therefore, the introduction of contrast agents that shorten T_2 enhances negative contrast, making lesions or specific regions where contrast agent accumulates, darker. For the T_1 contrast agent the regions of higher contrast accumulation are brighter in T_1-weighted images.

Adjusting the pulse sequence parameters, such as TR and TE, allows for optimization of contrast for different imaging applications.

2.5.2 Signal Intensity in Multi-Echo and RARE Imaging

The NMR signal in the multi-echo (ME) and RARE pulse sequence is provided by the following equation [1]:

$$S \propto \left(1 - e^{\frac{-TR}{T_1}}\right) e^{\frac{-TE}{T_2}} \tag{2.15}$$

where S is the signal intensity, T_1, T_2 are relaxation times, TR is the repetition time and TE is the echo time. As seen from the equation a shorter T_2 relaxation time results in faster signal decay. The ME pulse sequence can be used for T_2 measurements, when TR is long enough to remove T_1 effect although residual T_1 weighting can still may influence signal decay.

2.5.3 Signal in IR FISP Imaging

The IR FISP combines inversion recovery with gradient echo steady state free precession to enhance T_1 contrast while maintaining rapid acquisition. When low flip angle pulses α and TR << T_1 are used pulse IR FISP can be used for T_1 quantification. The signal in an IR FISP pulse sequence can be expressed as [27]:

$$S = M_0 \left[\frac{T_1^*}{T_1} - \left(1 + \frac{T_1^*}{T_1}\right) e^{\frac{-t}{T_1^*}}\right] \tag{2.16}$$

Where T_1^* is the apparent longitudinal relaxation time and can be seen in the equation below:

$$T_1^* = \left[\frac{1}{T_1} - \frac{1}{TR}\ln(\cos(\alpha))\right]^{-1} \quad 2.17$$

Equation 2.16 can be written as:

$$S(t) = A - Be^{\frac{-t}{T_1^*}} \quad 2.18$$

Where A, B, and T_1^* can be obtained by three parameter fitting, hence T_1 can be calculated as:

$$T_1 = T_1^*\left(\frac{B}{A} - 1\right) \quad 2.19$$

2.5.4 Relationship between Signal Intensity, Relaxation Times and Pulse Parameters in MRI

MRI is likely the most complex of all imaging techniques. As presented above, there are many pulse sequences and many associated parameters, that allow imaging of complex properties of tissues such as relaxation times. The selection of the pulse sequence and its parameters drastically changes MR image, including resolution, contrast, SNR etc [23]. Hence, MRI requires a comprehensive understanding of its principles, unlike other methods such as computed tomography (CT) or positron emission tomography (PET), that require very little adjustments and provide similar type of images independent of settings.

In MRI, while T_1 and T_2 relaxation times are inherent properties of tissues and are critical in providing MRI contrast, they do not alone determine how signal appears in an image. Selection of a pulse sequence and its parameters significantly impact image contrast and quality.

For instance, to obtain maximum contrast between two tissues with different T_2 values selection of proper TE and long TR must be applied, while to differentiate tissues based on T_1

values TR is must be properly selected while TE should be short. Additionally, subtle imperfections such as B_0 field inhomogeneities, gradient non-linearities, patient movement, implants or blood flow can degrade the signal. Furthermore, RF noise due to insufficient shielding or aliasing due to incorrect selection of the field of view can all spoil the image [23].

Chapter 3 – Contrast Agents

Contrast agents used in MRI reduce relaxation times of surrounding protons due to their magnetic properties. The relaxation effects of paramagnetic and superparamagnetic materials in MRI arise from interactions between water protons and unpaired electron spins. The contrast agents accelerate the relaxation of water protons in the tissue where they accumulate, providing better differentiation between healthy and abnormal tissues increasing the diagnostic capabilities of MRI. Contrast agents are comprised of materials, that exhibit distinct behaviour when placed in the magnetic field.

The magnetic field within the material can be induced by the external magnetic field H according to the formula:

$$M = \chi H \qquad 3.0$$

where χ is the magnetic susceptibility of the material, M is the magnetization (A/m).

Based on the value of the susceptibility χ, materials can be divided into: diamagnetic materials ($\chi < 0$), for example water; paramagnetic materials ($\chi > 0$), such as gadolinium (Gd), and superparamagnetic materials ($\chi > 1$), such as iron oxide nanoparticles. When removed from the external magnetic field these materials return to their initial state. Ferromagnetic materials ($\chi >> 1$) such as nickel, store their magnetization even after removal from the magnetic field.

The magnetic properties are related to the electron distribution with atoms. Diamagnetic materials have no unpaired electrons, resulting in a weak and negative response to an external magnetic field. When placed in a magnetic field, the electrons within these materials slightly alter their orbits, creating small, opposing magnetic moments that resist the applied field. This effect is generally very weak compared to paramagnetic and superparamagnetic materials. Therefore, in MRI, diamagnetic materials have minimal impact on relaxation times, as their magnetic properties do not contribute significantly to altering the magnetic environment of nearby protons.

Paramagnetic materials, such as Gd-based compounds, possess unpaired electrons that align with an external magnetic field. This alignment creates fluctuating local magnetic fields that enhance T_1 relaxation by accelerating the recovery of nearby water proton magnetization, thereby shortening the T_1 relaxation time.

Superparamagnetic materials, such as iron oxide nanoparticles, exhibit a strong response to external magnetic fields due to their large magnetic moments. These moments create large local magnetic field inhomogeneities, which accelerate dephasing of nearby water proton spins. As a result, T_2 relaxation can be significantly shortened, leading to signal loss in T_2-weighted MRI within tissues contrast agents accumulate in.

The theory of the nuclear relaxation in the presence of dissolved paramagnetic substances, called proton relaxation enhancement, was developed by Bloembergen, Solomon and others [28] based on research carried out by Felix Bloch, who showed enhancement of the relaxation of water protons in the presence of ferric nitrate [5].

Contrast agents used in MRI should meet the following requirements [29, 30, 31]:

1. Provide maximum relaxivity.
2. Should selectively accumulate in a targeted tissue.
3. Have minimum toxicity.
4. Must remain stable *in vivo* without significant dissociation.
5. Should be excreted within a few hrs to 24 hrs of administration.

3.1 T_1 Contrast Agents

T_1 contrast agents are more frequently used than T_2 contrasts as they provide strong signal enhancement on T_1-weighted images unlike T_2 contrasts that decrease signal on T_2-weighted images. Currently, the most common T_1 contrast agents are Gd-based. They are used in about 30% of MRI clinical scans to improve various disease detection, including breast, brain or prostate cancers [32].

Because Gd ions are toxic they are used as contrast agents synthetized with chelates, such as diethylenetriaminepentaacetic acid (DTPA), gadopentetate dimeglumine or gadoterate meglumine [33]. Gd-based contrast agents accumulate in cancer tissue due to the enhanced permeability and retention effect (EPR) when administered intravenously. EPR refers to the tendency of contrast agents to accumulate in tumor tissue more than in normal tissues [27] due to tumor's leaky vasculature and poor lymphatic drainage, allowing the contrast agents to penetrate and remain within tumor. These agents are primarily excreted from the body via kidneys through a process involving glomerular filtration. This process is complex and involves potential retention in the body, especially in patients with impaired renal function [27].

Gd-based ions are excellent contrast agents due to their strong paramagnetic properties, which significantly enhance the relaxation rates of nearby water protons. This effectiveness stems from Gd atom's electronic structure, specifically the seven unpaired electrons in its 4f orbital. These unpaired electrons create a strong magnetic moment, making Gd highly paramagnetic and enabling strong interaction with the external magnetic field, such as the one produced by an MRI scanner. When Gd chelate is introduced into the body, it shortens the T_1 relaxation time of nearby protons, which causes tissues with Gd to appear brighter on T_1-weighted images, thereby enhancing the contrast between tissues. While Gd also has some impact on T_2 relaxation, it primary effects T_1 relaxation [33].

3.2. T_2 Contrast Agents

T_2 contrast agents produce anisotropic variable magnetic field gradients which dephase the transverse magnetization causing reduction of T_2 relaxation times of the surrounding protons causing negative contrast enhancement (darker regions of accumulation in MR images). These contrast agents have rather small magnetic moments; however, they can induce transverse water proton spin relaxation with negligible induction of longitudinal water proton spin relaxation despite having low magnetic moments, thus acting as an efficient T_2 MRI contrast agent.

3.2.1 Iron-Based Contrast Agents

Iron oxide nanoparticles can be divided based on their size into superparamagnetic iron oxide nanoparticles (SPIO, size 50–500 nm) and ultra-small paramagnetic iron oxide nanoparticles (USPIO, size < 50 nm). SPIOs are the most frequently used T_2 contrast agents. They are highly effective MRI contrast agents due to their strong superparamagnetic properties. The effectiveness of iron oxide as a contrast agent is mostly attributed to 5 unpaired electrons per Fe^{3+} ion. These unpaired electrons create a substantial magnetic moment, resulting in a strong local magnetic field. When introduced into a water sample or a body, iron oxide particles cause significant dephasing of nearby water protons, leading to a rapid loss of phase coherence and a reduction of signal intensity in T_2-weighted images. This causes tissues containing iron oxide to appear darker on T_2-weighted MRI scans, enhancing the contrast between different tissues, for example in the detection of liver lesions or lymph nodes. Iron oxide particles can be coated with biocompatible materials, such as polyethylene glycol [34-35] to enhance their stability and circulation time in the body, further improving their effectiveness as contrast agents. These contrast agents exhibit an affinity for the cells of the liver's reticuloendothelial system (RES), where they are absorbed through phagocytosis. Overall, the combination of iron oxide's strong superparamagnetic properties hence its ability to cause significant T_2 decrease makes it an excellent choice for enhancing contrast of abnormalities such as liver, breast, prostate, brain or ovarian tumors [13][29].

In the thesis the iron-based H_2N-Fe_3O_4 contrast agent was used [36]. This contrast agent comprises azanide (H_2N) and magnetite (Fe_3O_4). Unlike standard iron based contrasts, it reduces both relaxation times T_1 and T_2 [36-37]. Within this thesis the relaxivities of H_2N–Fe_3O_4 in water at 9.4T and 3T were measured to evaluate its efficacy as a potential MRI contrast agent. Two magnetic fields were applied to evaluate suitability of the contrast for pre-clinical (9.4T) and clinical (3T) applications. The H_2N–Fe_3O_4 nanoparticles were applied in the animal model of prostate cancer using a 9.4T MRI system. The T_1- and T_2-weighted images were acquired before and after injection of the contrast agent.

3.2.2 Dysprosium-Based Contrast Agents

Dysprosium (Dy) is a rare earth element and has magnetic properties suitable for its application in MRI as a T_2 contrast agent. Dy has a high (but not very high compared to other ions) magnetic moment due to its unpaired electrons in the 4f orbital. Therefore, it has a strong transverse relaxivity (r_2) with a negligible longitudinal relaxivity (r_1). This property leads to rapid dephasing of nearby water protons, which darkens the tissue areas containing Dy in T_2-weighted MRI images, enhancing the contrast between different tissues.

To reduce toxicity, Dy-based contrast agents are typically synthesized with chelating agents, such as DTPA and other ligands that ensure stability and safety upon administration [31]. When administered intravenously, Dy-based contrast agents can accumulate in certain tissues, particularly in tumors, due to the EPR effect [9, 11, 38-39].

3.3 Core-shell Paramagnetic Contrast Agents

A core-shell nanoparticle is a type of composite material with the core material surrounded by the shell with different magnetic properties. Recent advances in nanotechnology allowed reproducible production of core-shell based contrast agents. This progress in nanotechnology allowed synthesis of nanoparticles comprising T_1 and T_2 shortening material as shell and core or vice versa. Independent modification of the core and shell provides controlled relaxivities r_1 and/or r_2. This independent fine tuning of r_1 and r_2 by changing the size or/and composition of the core and shell enhances image contrast utilizing both T_1 and T_2 shortening effect. Beyond changing relaxation times, the shell can be modified to enable other functions. For instance, functionalization of the shell allows synthesis of specific ligands or biomolecules, which can increase the contrast agent's specificity by targeting tissues or cells [40]. Further modifications of the shell can improve biocompatibility, ensuring that the contrast agent is well tolerated by the body and reducing the risk of adverse immune reactions. Additionally, stability can be enhanced through surface coatings with PEG (polyethylene glycol), in so called PEGylation process, which protects the nanoparticles from aggregation and prolongs their circulation time in the bloodstream. Furthermore, contrast agents for other imaging modalities, such as CT or PET can be added to the core-shell nanoparticles expanding their diagnostic capability [41].

In this study $NaDyF_4$-$NaGdF_4$ core–shell nanoparticles were used as an MRI contrast agent. The contrast consists of a dysprosium core surrounded by a gadolinium shell. This nanoparticle is designed to fine-tune magnetic interactions between water molecules with core and shell offering potential for dual T_1 and T_2 contrast modulation. These nanoparticles were administered in an animal model of triple-negative breast cancer, and imaged with an MRI system operating at 9.4T. Both T_1- and T_2-weighted scans were acquired before and after administration to observe changes in signal intensity within tumor and the adjacent tissue.

3.4 Targeted Contrast Agents

The development of contrast agents conjugated with antibodies or other targeting molecules (called targeted contrast agents) allowed the contrast agent to selectively bind to molecular targets within tissues or cells. Coupling contrast agents with antibodies or other targeted molecules, increases the imaging contrast between normal tissues and specific tumors. This targeted approach provides greater clarity and accuracy in diagnosing diseases.

Furthermore, targeted contrast agents conjugated with antibodies show great potential in theranostics (diagnostic and therapeutic). Antibodies are used due to their high specificity to particular biomarkers, allowing precise localization of a disease. In addition to their imaging capabilities, the antibodies conjugated with contrast agents can serve as carriers for therapeutic drugs, offering a dual-function approach to disease imaging and treatment, enhancing both the diagnostic precision and therapeutic efficacy [56]. However, despite this technological breakthrough, challenges remain. Optimizing conjugation techniques, ensuring stability and minimizing immunogenicity and toxicity are critical issues that must be addressed before these agents can be widely adopted in clinical practice [42-45].

3.5 Current Methods of Prostate and Breast Cancer Diagnosis

Detection of prostate and breast cancer at an early stage significantly improves patient outcomes [46-47]. Prostate cancer screening commonly involves prostate specific antigen (PSA) testing and digital rectal examination (DRE). PSA testing lacks specificity, which can result in overdiagnosis and potential overtreatment [48]. DRE has low sensitivity, especially for tumors located in areas not easily accessible by touch [49]. Ultrasound, often used to guide

biopsies, provides limited soft tissue contrast and may miss clinically significant tumors [50]. These limitations highlight the importance of MRI in prostate cancer detection, offering enhanced visualization of prostate anatomy and improved tumor localization without the drawbacks associated with traditional methods [51-52].

Traditional screening methods for breast cancer, such as mammography and clinical breast examination, are widely implemented but have several drawbacks. Mammography, although considered the gold standard for population screening, relies on ionizing radiation and has reduced sensitivity in women with dense breast tissue - an issue that affects nearly 50% of the screening population [53]. In such cases, lesions may be obscured, resulting in false negatives or delayed diagnosis. Clinical breast exams and self-palpation can miss small or deep-seated tumors, and their diagnostic reliability is highly dependent on examiner experience. Blood based biomarkers for breast cancer, such as CA 15-3 or CEA, lack the sensitivity and specificity needed for early detection [54]. These limitations prompt more sensitive, high-resolution modalities, which can visualize tumors regardless of breast density and without the risks associated with ionizing radiation. MRI meets these requirements.

T_1- and T_2-weighted MRI has been used for diagnosis of various cancers [55]. In prostate cancer, high-resolution T_2-weighted images are essential for identifying tumors in the peripheral zone, while T_1-weighted images are more useful in detecting vascularity [52]. In breast cancer, T_1-weighted sequences are commonly used to delineate tumor boundaries and assess vascularity, whereas T_2-weighted images help differentiate cysts from tumors [56]. However, the contrast obtained solely with optimized MR imaging technique may be further improved with the application of contrast agents.

3.5.1 Prostate Cancer Detection

Prostate cancer is the second most common cancer in men worldwide and leading cause of cancer related deaths [47]. In 2020 alone, over 1.4 million new cases were reported globally, with more than 375,000 deaths [48]. Although many prostate cancers grow slowly, some forms are aggressive and can spread quickly if not detected early. Risk increases with age, family history and ethnicity [48]. Advanced-stage prostate cancer can be difficult to treat and is often associated with poor outcomes, especially once it spreads beyond the prostate. This highlights

the need for accurate, early diagnosis and effective tools for distinguishing between low-risk and high-risk disease [57].

Imaging modalities like MRI, particularly when combined with contrast agents such as Gd or iron oxide contrast agents are essential for prostate tumor detection. This is due to the fact, that contrast enhanced MRI allows better visualization of prostate tumor boundaries and evaluation of its vascularity.

Gd-based contrast agents are integral for imaging prostate cancer. By shortening T_1 relaxation times, Gd can improve the delineation of tumor regions and surrounding tissue to a high degree. The high contrast between tumors and normal tissues, especially in prostate cancer, allows for more precise identification of tumor boundaries, facilitating accurate staging and treatment planning. Due to the abnormal vascular characteristics of prostate tumors, Gd enhancement produces distinct signal differences, as prostate tumors often exhibit irregular blood flow and vasculature. This enhanced contrast is particularly valuable for detecting clinically significant prostate tumors that might otherwise be missed, thus improving diagnostic accuracy and reducing the risk of false negatives [45, 47].

Additionally, both SPION and Gd-based agents may be functionalized with targeting ligands, such as antibodies or peptides, that bind specifically to tumor-associated biomarkers like prostate-specific membrane antigen (PSMA). This targeted delivery increases local accumulation of the contrast agent within prostate tumors, thereby enhancing image contrast and improving lesion detectability. As a result, functionalized SPIONs and Gd agents offer a powerful strategy for increasing MRI sensitivity and accuracy in the early detection and characterization of prostate cancer [45].

3.5.2 Breast Cancer Detection

Breast cancer is the most common diagnosed cancer among women worldwide, and remains one of the leading causes of cancer related mortality [42]. In 2022, over approximately 2.3 million women were diagnosed with breast cancer globally, resulting 670,000 deaths [46, 58-59]. Early stages of breast cancer can be treatable but aggressive types such as triple negative breast (TNB) and human epidermal growth factor receptor 2 (HER2), positive tumors

can progress rapidly if not detected early, making the use of MRI and contrast agents vital for the detection of breast cancer.

Gd-based contrast agents are routinely used in breast MRI to enhance tumor visibility and improve diagnostic accuracy. Their T_1-shortening effect results in stronger signal intensity in regions of abnormal perfusion, which is commonly observed in malignant breast tissue. This enhancement helps to better distinguish breast tumors from surrounding tissue. This can be utilized in patients with dense breast tissue, where conventional mammography may struggle to differentiate between tumor and normal tissue [60]. Moreover, Gd-based agents can improve the characterization of tumor margins and help identify small lesions that might be missed on non-contrast imaging, contributing to better early detection and reduced false negatives in breast cancer screening [60].

In breast cancer imaging, Dy-based contrast agents are being investigated due to their strong T_2 shortening capabilities and potential to improve breast tumor visibility in T_2-weighted MRI. Unlike Gd contrast agents, which generate positive contrast, Dy-based agents create negative contrast causing signal voids in areas where the contrast agent accumulates, making the breast tumors more easily distinguishable from surrounding tissues. This can be particularly useful for imaging lesions that may not be well-differentiated using conventional positive contrast agents [60].

Targeted contrast agents are being developed to improve breast cancer detection by binding to specific tumor receptors overexpressed in breast cancer. Gd-based contrast agents functionalized with peptides or antibodies targeting these makers have demonstrated improved T_1-weighting imaging of TNB in preclinical models. Similarly, contrast agents containing Dy conjugated for TNB specific binding, show promising potential for enhancing T_2-weighted imaging [60]. These targeted agents provide a non-invasive mechanism to image, monitor and diagnose TNB to a greater degree than conventional, non-targeted contrast agents, by enabling selective accumulation within tumors.

Chapter 4 – Materials and Methods

4.1. Animal Models

Animal models of cancer are used to study cancer development and treatment efficacy *in vivo* as a necessary step before any human applications. There are two primary types of animal models: xenograft and genetically engineered mouse models (GEMMs). Xenograft models are created by injecting human cancer cells into nude mice, which lack a functional immune system due to a genetic mutation affecting T cell development. This lack of immune defence ensures successful growth of human tumors while limiting the ability to study immune cancer interactions. Nude mice are in an immunodeficient state which takes away the confounding effects of an adaptive immune system. GEMMs were developed by manipulating specific genes to induce tumor formation within their normal immune system, providing an information about cancer initiation and progression. GEMMs with mutations in genes TP53, MDA-MB-23TNB and HER2 are most often used in breast cancer models [61], while mutations in genes PTEN and P53 in prostate cancer models [62]. The choice between these models ultimately hinges on the research focus. The xenograft mouse models of prostate and breast cancer were used in the thesis, due to their ability to provide a robust platform to study human-specific cancer dynamics.

4.1.1 Animal Model of Prostate Cancer

For the prostate cancer model, six, five-week-old male athymic nude mice were used. Each mouse was subcutaneously inoculated on its flank with a suspension of $3x10^6$ PC3 cells, prepared in a 50:50 mixture of Matrigel and RPMI-1640 media supplemented with 10% fetal bovine serum and 1% antibiotics/antimycotics. Tumors were allowed to grow for approximately three weeks, reaching a size of about 5 mm in diameter. Once tumors reached the desired size, mice were administered the contrast agent via intravenous injection through the tail vein, followed by MR imaging [36].

4.1.2 Animal Model of Breast Cancer

In this studies of the TNB cancer model, six, six-week-old female athymic nude mice were used. Each mouse was orthotopically inoculated with $2x10^6$ MDA-MB-231 cells [60],

resuspended in 20 µl of sterile saline. The cells were prepared by culturing in RPMI-1640 medium supplemented with 5% fetal bovine serum. Tumors developed as solid spheroidal masses over three weeks, reaching a size of approximately 50 mm^3. Prior to implantation, cells were harvested by trypsinization, centrifuged, and resuspended for injection. The cells were implanted into the left #4 inguinal mammary gland of each mouse. Once tumors reached the desired size, mice were administered the contrast agent via intravenous injection through the tail vein, followed by MRI imaging [60].

4.2. Synthesis and Characterization of the Contrast Agents

Two types of nanoparticles were used as contrast agents: core-shell $NaDyF_4$-$NaGdF_4$ and $H_2N{-}Fe_3O_4$ for the breast and prostate cancer models respectively. The synthesis of the nanoparticles was performed by the Canadian and Taiwanese collaborators [36, 60].

Previous studies indicated very low toxicity of the H_2N-Fe_3O_4 nanoparticles [36, 45] showing kidney cells viability remain unchanged at dosages from 0.125 to 8 mM after 4 hrs of exposure. *In vitro* hemolysis using human blood showed only mild hemolysis g/dl at 0.1M iron concentration, which is much higher than required for an MR contrast enhancement. *In vivo* studies involving intravenous administration in mice showed no observable toxic effects, with histological analysis of major organs, including the liver, kidneys, spleen, heart and lungs, revealing no tissue damage [36].

A previous work showed low toxicity of $NaDyF_4$-$NaGdF_4$ contrast agents, demonstrating their safety and suitability for biomedical applications [60]. *In vitro* experiments revealed negligible cytotoxicity on mammalian cells at concentrations relevant for imaging. Hemolysis testing further indicated that these nanoparticles did not cause significant damage to red blood cells, confirming their compatibility with blood-based applications. *In vivo* studies involving intravenous injection in mice showed no detectable toxicity. Histological examinations of major organs, including the liver, kidneys, spleen, heart, and lungs, revealed no tissue damage [60].

4.2.1. Synthesis and Characterisation of H_2N-Fe_3O_4 Nanoparticles

The coprecipitation method [36] was used to synthesize the H_2N-Fe_3O_4 nanoparticles (Fig. 20). This approach involves the simultaneous precipitation of ferrous (Fe^{2+}) and ferric (Fe^{3+}) ions in an alkaline medium. The process allows control the particle size and composition by adjusting processing parameters, such as pH or temperature. This method is favored for its simplicity and efficiency in producing nanoparticles suitable for various applications [36].

Once H_2N-Fe_3O_4 nanoparticles were produced, alginates were bonded to its surface through a covalent linkage. In particular, 1.0 M ferric chloride hexahydrate ($FeCl_3 \cdot 6H_2O$) and 2.0 M ferrous chloride tetrahydrate ($FeCl_2 \cdot 4H_2O$) were separately prepared using 2.0 M HCl aqueous solutions. 2.0 mL of 2.0 M $FeCl_2$ solution and 8.0 mL of 1.0 M $FeCl_3$ solution were mixed, and then, 1.0 g of glycine was added. This solution was vigorously stirred for 5 min, and then, 5 M NaOH aqueous solution was slowly added until the solution turned from yellow to black. The solution was vigorously stirred for another 10 min at room temperature. The precipitates were collected using a permanent magnet, and the supernatant was removed. The precipitates were washed with deionized water. Subsequently, 3.0 g of glycine dissolved in 25 mL of deionized water was added, and the solution was then sonicated for 30 min. After sonication, deionized water and acetone were added into solution, and the solution was centrifuged at 10 000 rpm for 10 min. Finally, the precipitates were redispersed in deionized water to obtain the solution of NH_2-Fe_3O_4 nanoparticles [36].

An inductively coupled plasma (ICP) analysis was used to measure the Fe ion concentration for the NH_2-Fe_3O_4 nanoparticles, yielding 2 mgFe/cm^3 [36].

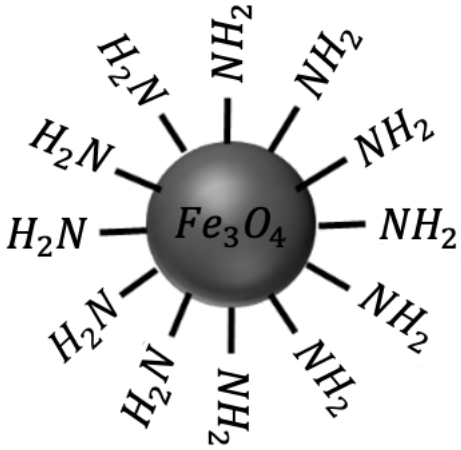

Fig. 20. *Schematic of the H_2N-Fe_3O_4 nanoparticle.*

Transmission electron microscopy (TEM) images showed the hydrodynamic diameters of H_2N-Fe_3O_4 nanoparticles to be 17 ± 2.1 nm (Fig. 21). The relaxivities r_1 and r_2 of the NH_2-Fe_3O_4 nanoparticles in an aqueous solution were found to be $r_1 = 0.11 \pm 0.02$ mM^{-1} s^{-1} and $r_2 = 3.8 \pm 0.54$ mM^{-1} s^{-1} respectively at 9.4T [36].

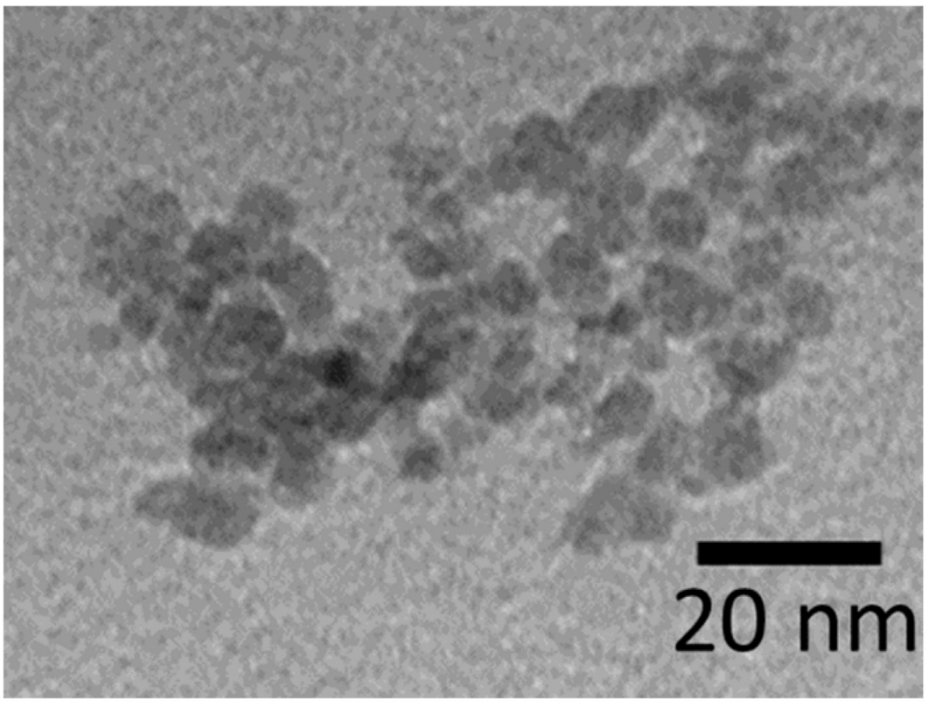

Fig. 21. *TEM images of the H_2N-Fe_3O_4 nanoparticles [36].*

4.2.2 Synthesis and Characterisation of the $NaDyF_4$-$NaGdF_4$ Contrast Agent

Prior to the synthesis of the core-shell nanoparticles, cubic-phase (α) $NaGdF_4$ nanoparticles were synthesized, which acted as the sacrificial nanoparticles for shell formation [45, 60]. The multi-step process of the cubic-phase (α) of sacrificial $NaGdF_4$ synthesis started from Gd oxide, via Gd trifluoroacetate, mixed with various chemicals, heating, washing, and cooling cycles. Finally, the nanoparticle precipitated and washed with ethanol and dispersed in hexane. To synthesize $NaDyF_4$, dysprosium (III) chloride hexahydrate was stirred in oleic acid and 1-octadecene under vacuum for 45 min at 120°C. Further steps included heating, cooling, and stirring solutions of methanol containing sodium hydroxide and ammonium fluoride. After removing methanol by heating, the previously synthesized sacrificial (α) $NaGdF_4$ nanoparticles

dispersed in 1-octadecene (1 ml) were injected into the solution and stirred for 15 min to form a core-shell nanostructure. The nanoparticles were precipitated and washed with ethanol, and then finally dispersed in hexanes [45, 60]. A schematic illustration of the final $NaDyF_4$-$NaGdF_4$ nanoparticle is shown below (Fig. 22):

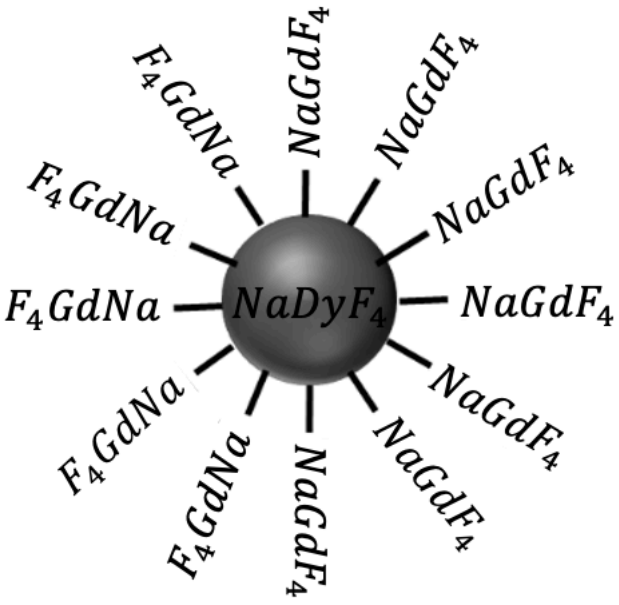

Fig. 22. *Schematic illustration of the $NaDyF_4$-$NaGdF_4$ nanoparticle.*

The synthesized $NaDyF_4$-$NaGdF_4$ nanoparticles were analyzed using the X-ray diffraction method (XRD), showing the standard pattern of the hexagonal phase (β) of the $NaDyF_4$ core. Analysis of the particle size distribution using the transmission electron microscopy (TEM) images showed a $NaGdF_4$ shell thickness of 0.6 ± 0.1 nm while the core $NaDyF_4$ nanoparticle showed a diameter of 21.2 ± 0.1 nm and the total core-shell nanoparticles had a diameter of 21.8 ± 0.1 nm. The relaxivities r_1 and r_2 of the $NaDyF_4$-$NaGdF_4$ nanoparticles in deionized water were $r_1 = 9.4 \pm 0.2\ mM^{-1}\ s^{-1}$ and $r_2 = 144.7 \pm 7.3\ mM^{-1}\ s^{-1}$ respectively. The TEM images can be seen in Figure 23 [45]:

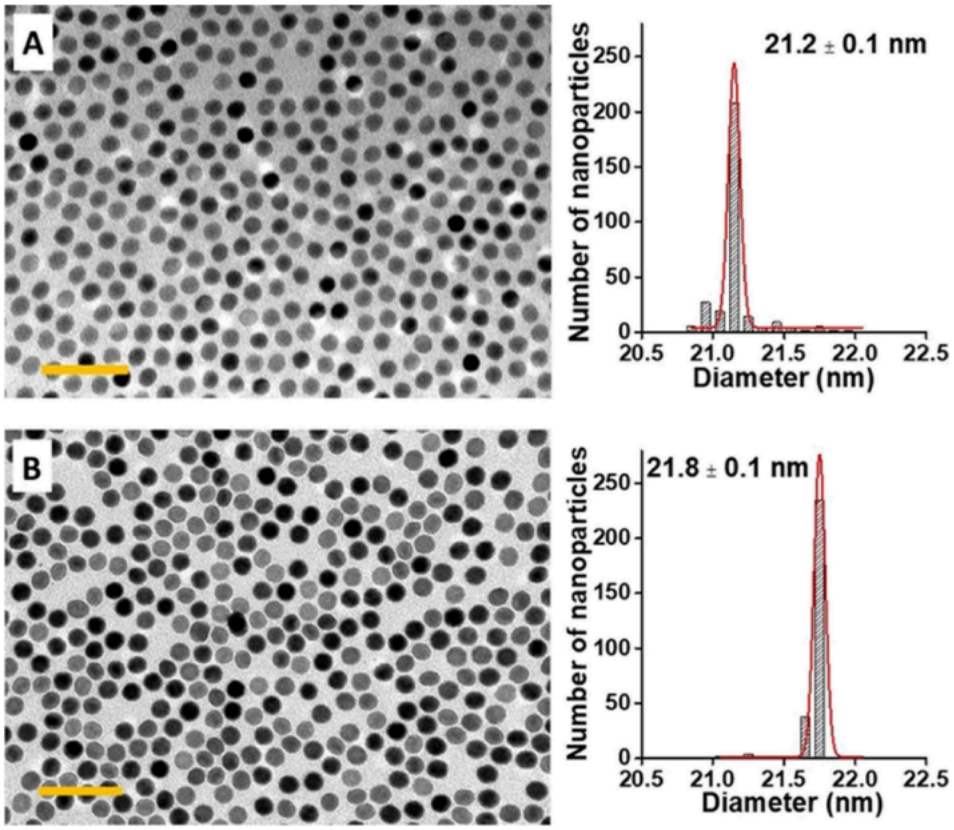

Fig. 23. *TEM images of the nanoparticles and their size distribution: (A) $NaDyF_4$ nanoparticles and (B) $NaDyF_4$−$NaGdF_4$ core−shell nanoparticles. Yellow scale bar indicates 100 nm. The core NaDyF4 is 21.2 ± 0.1nm and the total diameter including the NaGdF4 shell is 21.8 ± 0.1nm diameter [45].*

4.3 MRI Experiments

All the *in vivo* experiments were performed using the 9.4T, 21 cm bore MRI system (Bruker, Ettlingen, Germany). The mice were positioned prone inside the magnet, with a volume RF coil placed over the region of interest (ROI) namely the tumor. The relaxivity measurements were performed using a whole body 3T MRI system (Trio, Siemens, Germany), and the 9.4T, 21 cm bore MRI system.

4.3.1 MRI of Prostate Cancer

For the MRI prostate cancer scans, the animals were anesthetized with isoflurane (1.5-2% in 30% oxygen) administered through a nose cone, placed in a cradle positioned within the center of the bore of the magnet, and situated in the prone position. The animals were kept normothermic using a circulating water blanket and the pulse sequences were triggered with respiration. Imaging sessions were conducted before the injection and 12 min, 1 hr, 2 hrs and 24hrs after the injection of nanoparticles [36]. Each animal received an intravenous injection of H_2N-Fe_3O_4 nanoparticles at a concentration of 2 mg Fe/ml, redispersed in deionized water as described in Section 4.2.1. The injection vehicle was not modified prior to administration, and no acute adverse effects were observed..

For the prostate cancer T_1- and T_2- weighted images were obtained with the IR FISP [36] and MSME pulse sequence, respectively. The IR FISP pulse sequence parameters were: TE = 1.5ms, TR = 3 ms, TI = (305.5 - 11441.5) ms, flip angle (FA) = 60 deg, matrix size 128 x 256, FOV 2.56 cm x 3.0 cm, slice thickness 1mm.

Parameters of the T_2 weighted MSME pulse sequence were: TE = 35 ms, TR = 5000 ms, FOV = 2.56 × 3 cm, slice thickness 1 mm, matrix size 128 × 256. The relatively long TE and long TR in the MSME pulse sequence allows T_2 -weighing [36].

4.3.2 MRI of Breast Cancer

For the MRI breast cancer animal model, anesthesia was induced with 4% isoflurane and maintained with 2.7% isoflurane in 69% N_2O and 30% O_2, administered through a nose cone, placed in a cradle positioned within the center of the bore of the magnet, and situated in the supine position. The animals were kept normothermic using a circulating water blanket and the pulse sequences were triggered with respiration. Imaging sessions were carried out before the injection, 15 min, 1 hr, and 2 hrs after the injection of nanoparticles. Each mouse received a 250 µl tail vein injection of contrast agent suspended in 0.9% saline [60].

For the breast cancer T_1- and T_2- weighted images the inversion recovery with RARE and MSME pulse sequence was used, respectively. For T_1 measurements, the RARE sequence

parameters were: TE = 7ms, TR = 750ms, 1 slice, matrix size 512 × 96, FOV = 5.12 × 2.56 cm, slice thickness 1mm. The relatively short TR provides T_1 weighting, while short TE reduces T_2 relaxation effect in MR images.

For the T_2-weighted MSME pulse sequence the following parameters were used: TE = 5 ms, TR = 5000 ms , matrix size 128 × 128, FOV 2.56 cm × 3.0 cm, slice thickness 1 mm. The long TR in the MSME pulse sequence allows the longitudinal magnetization to fully recover, minimizing T_1-weighting.

The signal intensity data were analyzed using Python (Centrum Wiskunde & Informatica, Amsterdam, The Netherlands) version 3.6. *In vivo* relaxation times were calculated in Paravision ver 5.1 (Bruker, Germany).

4.3.3 Phantom Tumor Model

To assess enhancement of the tumor cancer signal in MRI using contrast agents, a theoretical analysis of signal changes in T_1-weighted and T_2-weighted MR images was performed. Application of T_1, T_2, and dual-mode (T_1/T_2) agents was analyzed. In this model, the tumor is surrounded by a normal tissue, with both regions represented as homogeneous ellipses (Fig. 24). Tumor contrast (TC) was defined as the ratio of the average signal intensity within the tumor area to that in the surrounding tissue:

$$\mathrm{TC} = \frac{S_{tu}}{S_{ti}} \qquad 4.0$$

where S_{tu} and S_{ti} are the signal intensities of tumor and tissue.

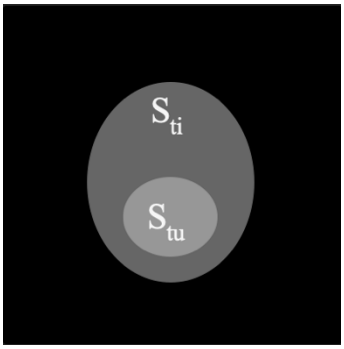

Fig. 24. *An artificial image of a phantom tumor model comprising tumor (S_{tu}) surrounded by a normal adjacent tissue (S_{ti}) used for contrast analysis.*

The theoretical ("ideal") tumor model is based on prior MRI studies of cancer, particularly breast cancer [63]. The previous states reported approximately a 50% enhancement in TC following contrast agent administration. This model does not take into account *in vivo* factors such as heterogeneous agent uptake, metabolic activity, tumor progression, agent concentration. It also does not analyze pulse sequences. The model focuses on changes in TC after contrast injection due to shortening of T_1 and T_2 relaxation times.

In particular, both the tumor and surrounding tissue were initially assigned identical signal intensities: 100 arbitrary units (au) in T_1-weighted images and 70 au in T_2-weighted images as previous MRI studies showed these values in breast images [63]. An "ideal", tumor contrast agent accumulates exclusively within the tumor region. For a T_1 agent, 50% signal increase within the tumor only was assumed, with no change in the adjacent tissue. Conversely, tumor signal decreases 50% due to a T_2 agent injection, again with no effect on the surrounding tissue. For a dual-mode (T_1/T_2) agent, a 50% increase in T_1-weighted and a 50% decrease in T_2-weighted signal intensities within the tumor [64]. Finally, images were subtracted to investigate possible improvement in tumor contrast using image post-processing [Table 2] [60]. The corresponding images are shown in Figures 25 to 28. The details of the investigation are provided in ref [60].

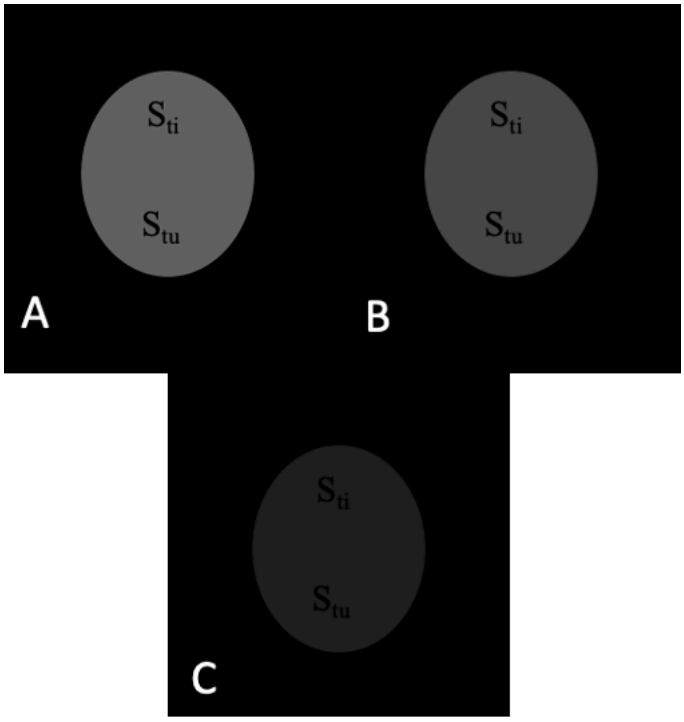

Fig. 25. *Theoretical images of the tumor phantom model before contrast injection based on the values in Table 2: (A) T_1-weigthed; (B) T_2-weighted; (C) Subtracted $T_1w - T_2w$. TC = 1.00 in all images.*

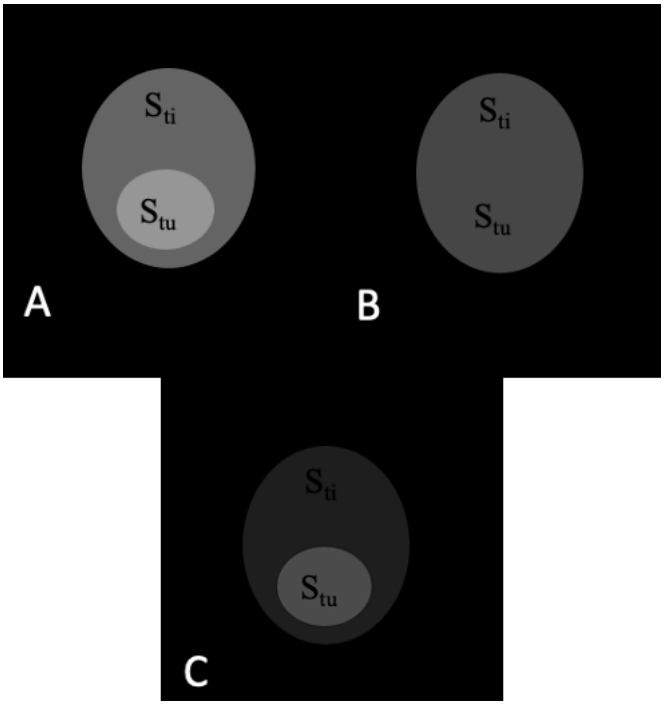

Fig. 26. *Theoretical MR images of the tumor phantom model after injection of a T_1 contrast agent: (A) T_1w, TC = 1.5; (B) T_2w, TC = 1; (C) subtracted T_1w- T_2w, TC = 2 (highest TC value).*

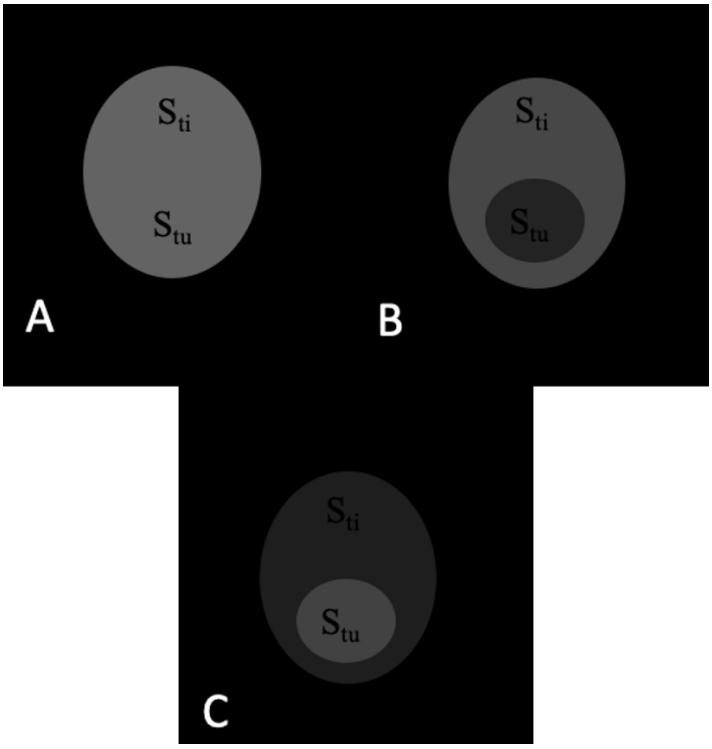

Fig. 27. *Theoretical MR images of the tumor phantom model after injection of a T_2 contrast agent: (A) T_1w, TC = 1; (B) T_2w, TC = 0.47; (C) TC = 2.17 (highest value) for subtracted T_1w- T_2w.*

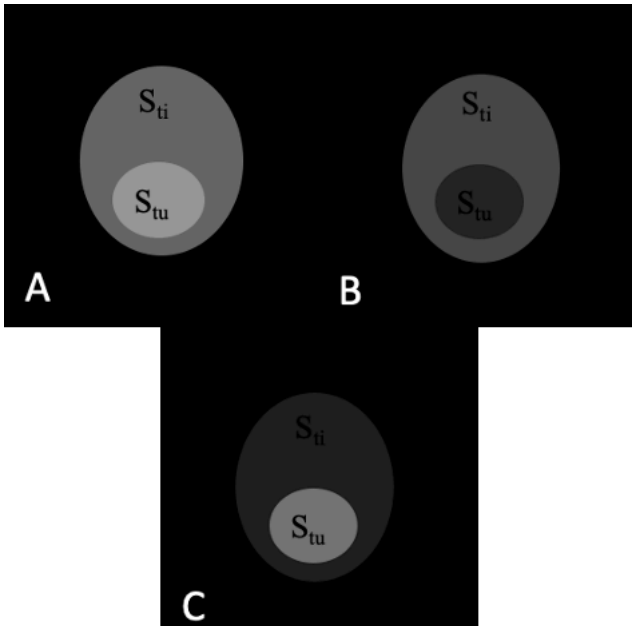

Fig. 28. *Theoretical MR images of the tumor phantom model after injection of the T_1/T_2 contrast agent: (A) T_1w TC = 1.5; (B) T_2w TC = 0.5; (C). Subtracted T_1w- T_2w TC = 3. The highest TC value of 3.0 is in the subtracted images (C).*

Table 2 shows the calculated signal intensities for the phantom tumor model. These results present signal intensities in images before and post-injection of a T_1, T_2 and T_1/T_2 contrast agents. The pre-injection tumor contrast TC was assumed to be equal 1.00 in all images (T_1- and T_2-weighted as well as in subtracted images), namely tumor and normal tissue had the same signal providing no contrast, as seen in Figure 25.

		$\mathbf{S_{tu}}$	$\mathbf{S_{ti}}$	TC
Pre-injection	T_1w	100	100	1.00
	T_2w	70	70	1.00
	$T_1w - T_2w$	30	30	1.00
Post-T_1 contrast injection	T_1w	150	100	1.50
	T_2w	70	70	1.00
	$T_1w - T_2w$	80	30	2.67
Post-T_2 contrast injection	T_1w	100	100	1.00
	T_2w	35	70	0.47
	$T_1w - T_2w$	65	30	2.17

Post-T_1/T_2 contrast injection	T_1w	150	100	1.50
	T_2w	35	70	0.50
	$T_1w - T_2w$	115	30	3.83

Table 2. *The signal intensities values of the tumor (S_{tu}) and normal tissue (S_{ti}) obtained from the phantom model. The tumor contrasts (TC) are shown for each image (T1-weigthed, T2-weighted and subtracted T1w-T2w) before and after the application of the "perfect" T_1, T_2, and T_1/T_2 contrast agents.*

The TC values vary in T_1-weighted (T_1w), T_2-weighted (T_2w), and subtracted $T_1w - T_2w$ images after injection of contrast agents. For figure 26 A-C the T_1 contrast agent, TC values are: 1.50, 1.00, and 2.67 in T_1w, T_2w and $T_1w - T_2w$ images, respectively. The highest TC = 2.67 is visible in the subtracted image (Fig. 26C). For figure 27 A-C the TC values change after injection of the T_2 contrast agent and are as follows: 1.00, 0.47, and 2.17 in T_1w, T_2w, and $T_1w - T_2w$ images, respectively. The highest TC = 2.17 value is visible in the subtracted images (Fig. 27C). Figure 28 A-C shows the TC values change after injection of the T_1/T_2 contrast agent and are: 1.50, 0.50, and 3.83 in T_1w, T_2w, and $T_1w - T_2w$ images, respectively. The highest TC = 3.83 value can be seen in the subtracted images (Fig. 28C).

In summary, the highest TC in each case was obtained when images were subtracted, and the highest TC overall was produced by the T_1/T_2 contrast agent (Fig. 28C). The post-processing allowed more than double (from 1 to 3.83) the tumor contrast when T_1/T_2 contrast agent was used along with the processing.

Chapter 5 – Results

This chapter presents the results of the relaxivity measurements of the H_2N-Fe_3O_4 nanoparticles (NPs) measured at 9.4T and 3T in aqueous solutions as well as *in vivo* studies of H_2N-Fe_3O_4 NPs in the prostate cancer model and $NaDyF_4$-$NaGdF_4$ NPs in the breast cancer model using the 9.4T pre-clinical MRI system. These animal models were used to evaluate the effectiveness of H_2N-Fe_3O_4, and $NaDyF_4$-$NaGdF_4$ NPs as contrast agents for MRI. Furthermore, an image post-processing method in the *in vivo* studies of $NaDyF_4$-$NaGdF_4$ contrast agent at 9.4T is demonstrated.

5.1 Relaxivity Measurement of the H_2N-Fe_3O_4 Nanoparticles in Water

Relaxivities (r_1 and r_2) of H_2N-Fe_3O_4 nanoparticles were calculated using a linear fitting of the relaxation rates $1/T_1$ and $1/T_2$ obtained from T_1 and T_2 measurements at different concentrations, at 9.4T and 3T according to Eqs. 1.33 and 1.34 (page 18).

5.1.1 Relaxivity of H_2N-Fe_3O_4 Nanoparticles in Aqueous Solution at 9.4T

Figure 29 presents $1/T_1$ and $1/T_2$ relaxation rates versus concentration for H_2N-Fe_3O_4 NPs measured at 9.4T. The linear data fitting provided the following relaxivities $r_1 = 0.11 \pm 0.02$ $mM^{-1}s^{-1}$ and $r_2 = 3.8 \pm 0.5$ $mM^{-1}s^{-1}$.

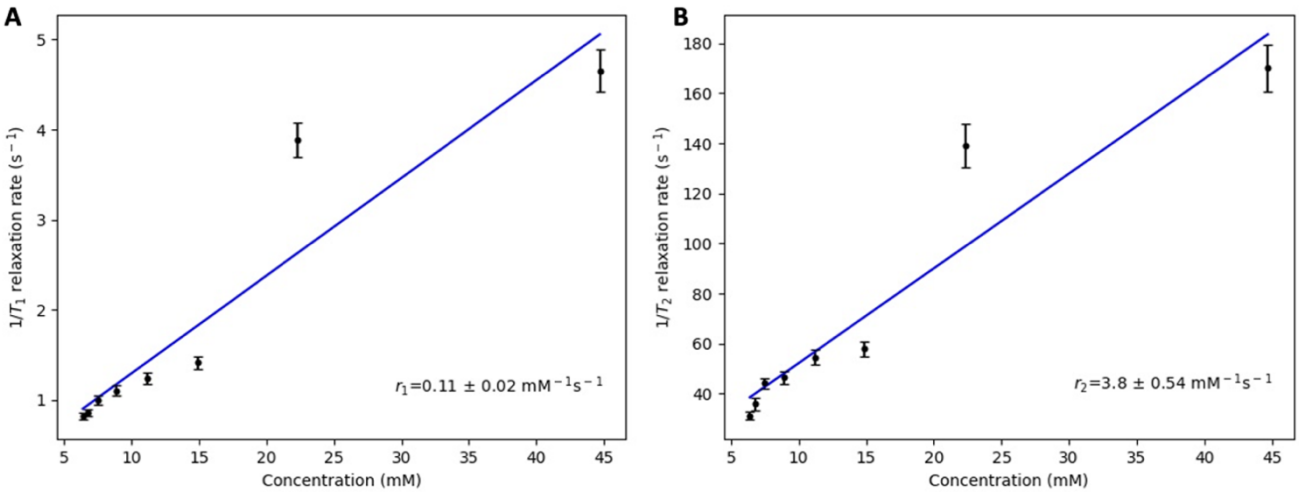

Fig. 29. *Relationship between the relaxation rates (A) $1/T_1$ and (B) $1/T_2$ of H_2N-Fe_3O_4 nanoparticles and their concentrations in water at 9.4T. The respective relaxivities are: r_1 = 0.11 ± 0.02 $mM^{-1}s^{-1}$ and r_2 = 3.8 ± 0.5 $mM^{-1}s^{-1}$.*

As seen from the results, $r_2 > r_1$ hence the expected the iron oxide-based contrast agent behaves mostly as a T_2 contrast. The observed relaxivity values support the potential use of H_2N-Fe_3O_4 as an effective T_2 agent as it provides strong T_2 reduction. If the contrast selectively accumulates in tumor, the reduction of signal in T_2-weighted images is stronger than in the surrounding tissue, hence provides a negative MRI contrast in T_2-weighted images.

5.1.2 Relaxivity of H_2N-Fe_3O_4 in Aqueous Solution at 3T

Figure 30 shows $1/T_1$ and $1/T_2$ relaxation rates versus concentration for H_2N-Fe_3O_4 NPs measured at 3T. The linear data fitting provided the following relaxivities: $r_1 = 0.44 \pm 0.01$ $mM^{-1}s^{-1}$ and $r_2 = 3.0 \pm 0.8$ $mM^{-1}s^{-1}$.

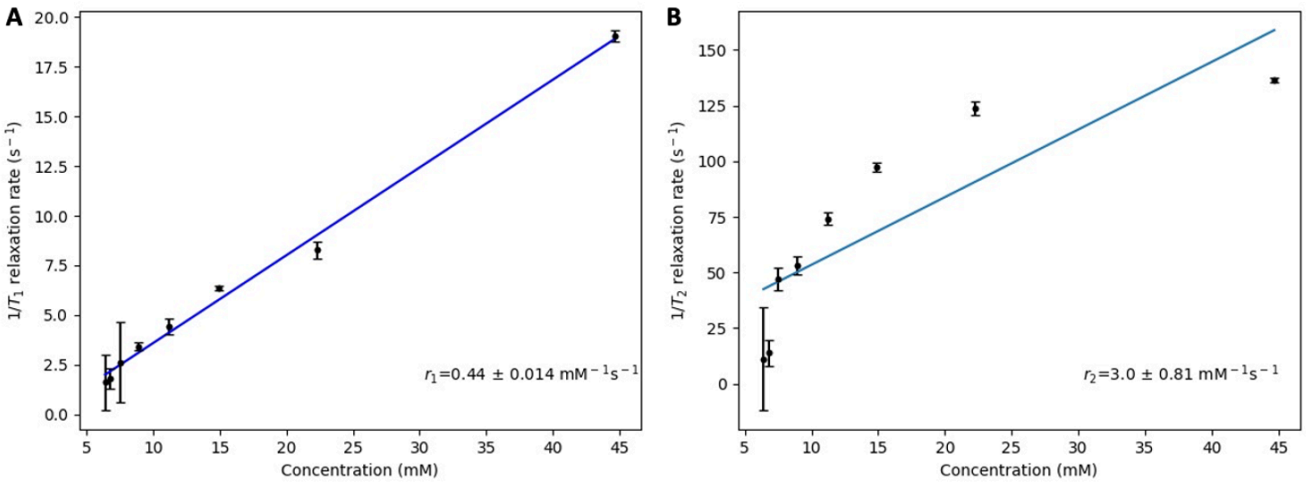

Fig. 30. *Relationship between the relaxation rates (A) $1/T_1$ and (B) $1/T_2$ of H_2N-Fe_3O_4 nanoparticles and their concentrations in water at 3T. The respective relaxivities are: r_1 = 0.44 ± 0.01 $mM^{-1}s^{-1}$ and r_2 = 3.0 ± 0.8 $mM^{-1}s^{-1}$.*

Comparison of r_1 and r_2 at 9.4T and 3T shows that r_1 is 4 times higher at 3T (*0.44 ± 0.01 $mM^{-1}s^{-1}$*) than at 9.4T (*0.11 ± 0.02 $mM^{-1}s^{-1}$*). The difference in r_2 is much smaller at different fields: *3.8 ± 0.5 $mM^{-1}s^{-1}$* at 3T and *3.0 ± 0.8 $mM^{-1}s^{-1}$* at 9.4T.

5.2 MRI of the Prostate Cancer Model using H_2N-Fe_3O_4 Contrast Agent

This section presents the *in vivo* application of H_2N-Fe_3O_4 NPs as a contrast agent for prostate cancer (PC3) imaging, across six animals. MRI scans were performed before, 12 min, 1 hr and 2 hrs after injection to monitor relaxation time changes in the tumor and adjacent tissue. The T_1- and T_2-weighted images were collected and analysed. Examples of T_1- and T_2-weighted MR imaging of one animal are provided in Figures 30 and 31.

Figure 30 shows the T_1-weighted MR images of a mouse bearing PC3 prostate tumor pre-injection (A), 12 min (B), 1 hr (C), 2 hrs (D) and 24 hrs post-injection (E) of the H_2N-Fe_3O_4 nanoparticles at the concentration of 2 mgFe/ml obtained at 9.4T.

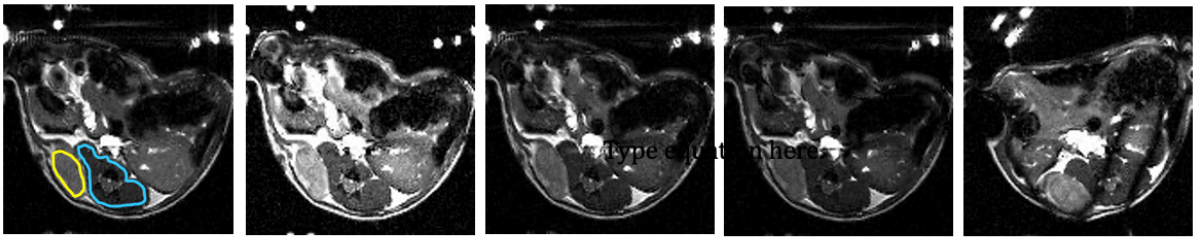

Fig. 30. *T_1-weighted MR images of a mouse bearing PC3 prostate cancer obtained at 9.4T before the injection (A), 12 min (B), 1 hr (C), 2 hrs (D) and 24 hrs (E) after injection of the H_2N-Fe_3O_4 nanoparticles contrast agent. The ROIs encompassing the tumor and tissues are marked with yellow and blue color respectively in (A) only for clarity.*

Figure 31 shows the T_2-weighted MR images of a mouse bearing PC3 tumor pre-injection (A), 12 min (B), 1 hr (C), 2 hrs (D) and 24 hrs post-injection of the H_2N-Fe_3O_4 nanoparticles at the concentration of 2 mgFe/ml obtained at 9.4T.

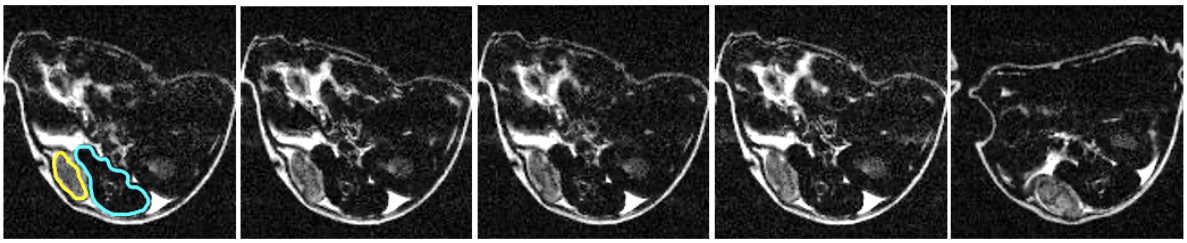

Fig. 31. *T_2-weighted MR images of a mouse bearing PC3 obtained at 9.4T before the injection (A), 12 min (B), 1 hr (C), 2 hrs (D) and 24 hrs (E) after injection of the H_2N-Fe_3O_4 nanoparticles. The ROIs encompassing the tumor and tissues were manually selected and marked with yellow and blue color respectively in (A) only for clarity.*

Because T_1 and T_2 relaxations vary among animals prior injection, to analyze the images, the changes in relaxations were normalized by calculating the relative signal intensity change ($RC_{1,2}$) as follows:

$$RC_{1,2} = \left(\frac{\bar{T}_{1,2}(t)}{\bar{T}_{1,2}(0)}\right) x100 \qquad 5.1$$

where $\bar{T}_{1,2}(0)$ and $\bar{T}_{1,2}(t)$ are the averaged T_1 and T_2 relaxation times across all six animals at time 0 and t respectively. RC was calculated for both PC3 tumor and normal tissue within ROI.

Figure 32 shows the $RC_{1,2}$ values over all six animals for T_1 and T_2 within tumor and tissue before, 12 min, 1 hr, 2 hrs and 24 hrs after injection.

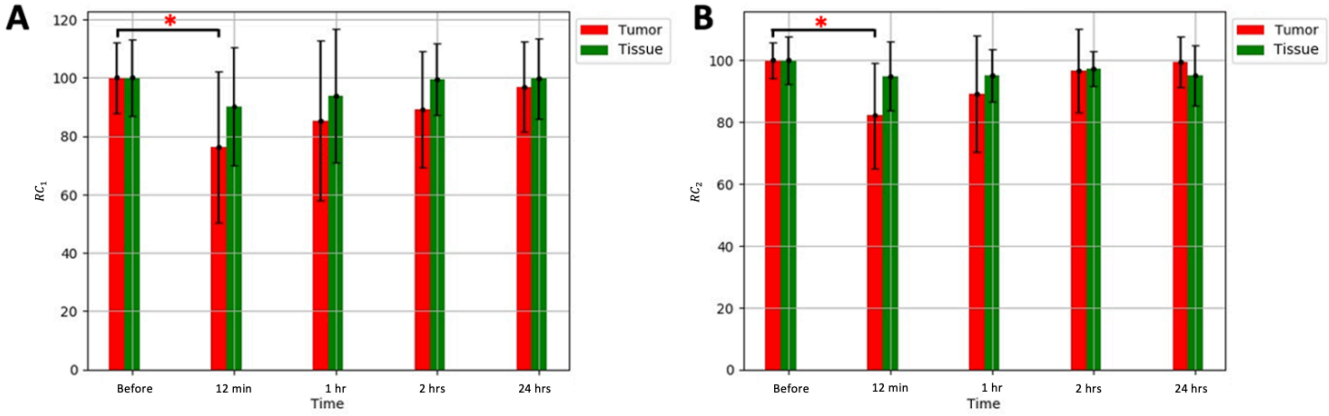

Fig. 32. *The relative changes ($RC_{1,2}$) over 6 animals in T_1 (A) and T_2 (B) relative relaxation changes within tumor and normal tissue before, 12 min, 1 hr, 2 hrs and 24 hrs after injection of the H_2N-Fe_3O_4 nanoparticles. A statistically significant ($p < 0.05$) difference in T_1 and T_2 within the tumor 12 min after injection is visible. The decrease 1 hr, 2 hrs and 24 hrs after injection is visible in both tumor and normal tissue but is not statistically significant ($p > 0.05$). An asterisk * indicates statistically significant difference ($p < 0.05$)*

Figure 32 shows the $RC_{1,2}$ of T_1 and T_2 relaxation times due to contrast accumulation in tumor and normal tissue across all six animals. The T_1 RC_1 (Fig. 32A) of tumor decreased to 76 ± 26 (p = 0.038), 85 ± 27 (p = 0.12) and 89 ± 20 (p = 0.078) 12 min, 1 hr, and 2 hrs post-injection, respectively, across all six animals. The normal tissue exhibited the decrease to 90 ± 20 (p = 0.15), 94 ± 23 (p = 0.27), 99 ± 12 (p = 0.44) 12 min, 1 hr and 2 hrs post-injection respectively and these changes were not significant (p > 0.05). At 24 hrs both T_1 of tumor and tissue returned to the pre-injection value of 97 ± 16 (p = 0.14) and 100 ± 14 (p = 0.46) respectively.

Figure 32B shows the RC_2 of T_2 across all animals in tumor and normal tissue. The T_2 RC_2 of tumor decreased to 82 ± 17 ($p = 0.028$), 89 ± 19 ($p = 0.12$) and 97 ± 14 ($p = 0.30$) 12 min, 1 hr, and 2 hrs post-injection, respectively. The tissue exhibited a slight decrease to 95 ± 11 ($p = 0.059$), 95 ± 8 ($p = 0.75$), 98 ± 6 ($p = 0.17$) 12 min, 1 hr, 2 hrs post-injection respectively. These changes were not significant ($p > 0.05$). At 24 hrs T_2 RC of both tumor and normal tissue returned to the pre-injection value of 99 ± 8 ($p = 0.46$) and 95 ± 10 ($p = 0.12$) respectively. The RC in tumor T_1 and T_2 RC were significant ($p < 0.05$) 12 min after injection only.

The results show that the H_2N-Fe_3O_4 nanoparticles influenced both the T_1 and T_2 relaxation times in the tumor and normal tissue only shortly (12 min) after injection, indicating early uptake in the tumor. 24 hrs after injection the relaxations returned to the initial values, suggesting the H_2N-Fe_3O_4 nanoparticles were completely washed out.

5.3 Breast Cancer MRI Following Injection of the $NaDyF_4$-$NaGdF_4$ Contrast Agent

This section shows the *in vivo* application of $NaDyF_4$-$NaGdF_4$ contrast agent to triple negative breast cancer (TNB) imaging in the animal model. MRI scans were performed pre, 15 min, 1 hr and 2 hrs post injection to monitor the changes in relative signal intensities in the tumor and the adjacent tissue across six animals. T_1- and T_2-weighted images were obtained with a 9.4T MRI system and analysed.

Figure 33 shows T_1-weighted MR images of a mouse bearing TNB tumor pre-injection (A), 15 min (B), 1 hr (C) and 2 hrs (D) post-injection of the $NaDyF_4$-$NaGdF_4$ nanoparticles.

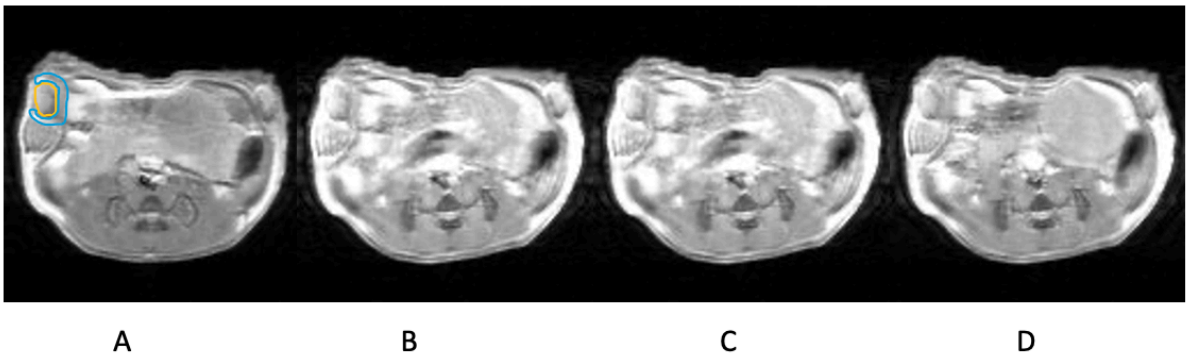

Fig. 33. *T_1-weighted MR images of a mouse bearing TNB cancer before the injection (A) and 15 min (B), 1 hr (C) and 2 hrs (D) after the injection of the $NaDyF_4$-$NaGdF_4$ nanoparticles.*

The ROI encompassing the tumor (yellow) and normal tissue (blue) have been manually selected and marked in (A) only for clarity.

Figure 34 shows T_2-weighted MR images of a mouse bearing TNB tumor pre-injection (A), 15 min (B), 1 hr (C) and 2 hrs (D) and post-injection of $NaDyF_4$-$NaGdF_4$ contrast agent.

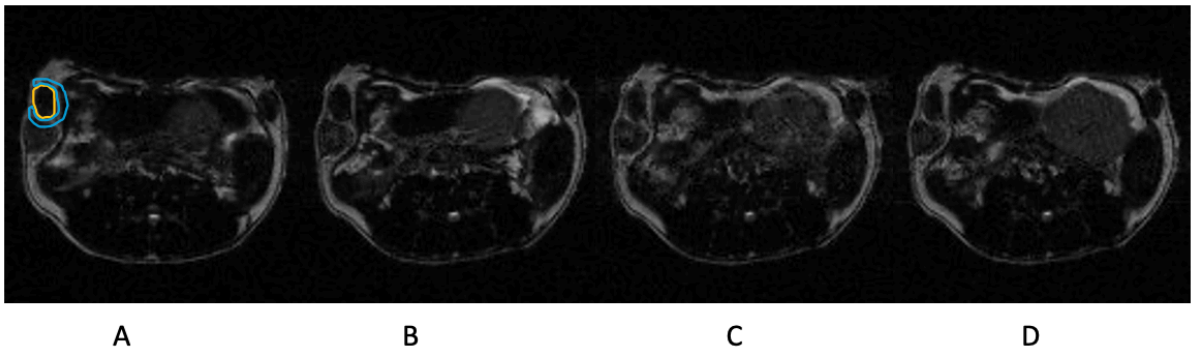

Fig. 34. *T_2-weighted MR images of a mouse bearing TNB cancer before (A), 15 min (B), 1 hr (C) and 2 hrs (D) after injection of the $NaDyF_4$-$NaGdF_4$ contrast agent. The regions of interest encompassing the tumor and tissue have been manually selected and marked as in Figure 34 (in (A) only for clarity) with yellow and blue colour, respectively.*

Since the signal intensity values of tumor and normal tissue vary among animals before the injection, the changes were normalized by calculating the relative change in signal intensities ($RIC_{1,2}$) in T_1- and T_2-weighted images, as follows:

$$RIC_{1,2} = \left(\frac{\bar{S}_{1,2}(t)}{\bar{S}_{1,2}(0)}\right) x100 \qquad 5.2$$

where $\bar{S}_{1,2}(0)$ and $\bar{S}_{1,2}(t)$ are the averaged signal intensities across all animals at times 0 and t, respectively, $\bar{S}_1$ and $\bar{S}_2$ are the average values of the signal intensities in T_1- and T_2-weighted images respectively. The $RIC_{1,2}$ was calculated for both the tumor and the normal tissue areas.

Figure 35 illustrates $RIC_{1,2}$ for the T_1-weighted and T_2-weigthed MRI across all animals, measured within the TNB tumor and the normal tissue before, 15 min, 1 hr and 2 hrs after injection of the $NaDyF_4$-$NaGdF_4$ contrast agent.

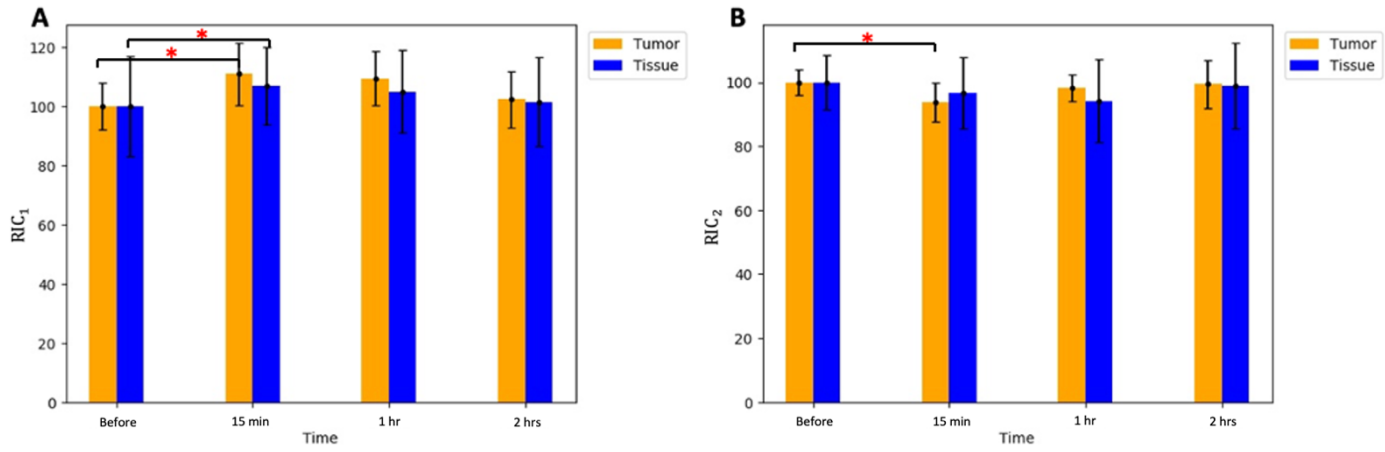

Fig. 35. *The averaged $RIC_{1,2}$ values over six animals for the T_1-weighted (A) and T_2-weighted MRI (B) within the TNB tumor and the normal tissue before, 15 min, 1 hr and 2 hrs post injection of the $NaDyF_4$-$NaGdF_4$ nanoparticles. The changes in tumor RIC_1 and normal tissue RIC_1 are significant ($p < 0.05$) 15 min after injection only. The changes in tumor RIC_2 are also significant ($p < 0.05$) 15 min after injection. An asterisk * indicates statistically significant difference ($p < 0.05$).*

Figure 35A shows the changes in RIC_1 due to contrast accumulation in tumor and normal tissue across six animals in T_1-weighted images. The RIC_1 of tumor increased from 100.0 ± 8.1 to 111.0 ± 10.5 ($p = 0.016$), then slightly decreased to 109.4 ± 9.2 ($p = 0.079$), and 102.3 ± 9.6 ($p = 0.26$) at before, 15 min, 1 hr and 2 hrs post-injection, respectively. The normal tissue RIC_1 increased from 100 ± 17.0 to 106.9 ± 12.9 ($p = 0.0047$), then slightly decreased to 104.9 ± 14.2 ($p = 0.15$) and 101.4 ± 14.8 ($p = 0.42$) before, 15 min, 1 hr, 2 hrs post-injection. The RIC_1 in tumor and normal tissue as well as RIC_2 in tumor were significant ($p < 0.05$) 15 min after injection.

Figure 35B shows the variations in RIC_2 due to contrast accumulation in both the tumor and normal tissue across six animals in T_2-weighted images. The RIC_2 of the tumor changed from 100 ± 3.9 to 93.8 ± 6.0 ($p = 0.030$), 98.2 ± 4.2 ($p = 0.24$) and 99.4 ± 7.4 ($p = 0.46$) before, 15 minutes, 1 hr and 2 hrs post-injection, respectively. The RIC_2 of the tissue changed from 100 ± 8.4 to 96.7 ± 11.6 ($p = 0.35$), 94.2 ± 12.9 ($p = 0.23$), and 98.91 ± 13.5 ($p = 0.44$) before at 15 minutes, 1 hr and 2 hrs post-injection, respectively. The RIC_2 in tumor was significant ($p < 0.05$) 15 min after injection in the tumor only. The $NaDyF_4$-$NaGdF_4$ nanoparticles caused

small (not statistically significant) changes in signal within the tumor and normal tissue 1 hr and 2 hrs after injection. These results suggest that uptake of the contrast agent within the tumor and tissue returned to the initial value, suggesting the $NaDyF_4$-$NaGdF_4$ nanoparticles were washed out.

5.4 Tumor/Tissue Image Post-Processing for the TC Enhancement in the Breast Cancer Model MRI

This section shows tumor contrast (TC) enhancement using the image post-processing, based on the theory presented in Chapter 4. Subtraction of a T_2-weighted from T_1-weighted image was applied to improve TC in a mouse model of TNB pre- and post-injection of the $NaDyF_4$-$NaGdF_4$ contrast agent.

Examples of the contrast enhancement in a mouse bearing TNB tumor obtained before and 15 min after the injection of the $NaDyF_4$-$NaGdF_4$ contrast agent are shown in Figure 36 and 37. Images marked with A, B, and C correspond to T_1w, T_2w, and subtracted T_1w − T_2w images, respectively. Signal intensity values S_{tu} and S_{ti} were calculated as the average pixel intensity within ROIs. TC was analyzed in T_1- and T_2-weighted MR images, as well as in subtracted (T_1w-T_2w) MR images, before and after contrast agent injection. The signal and TC values in each case are shown in Table 3.

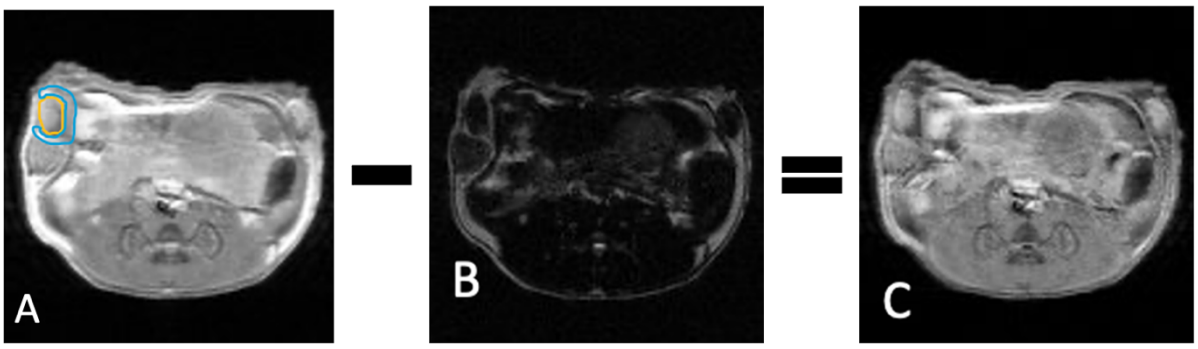

Fig. 36. *MR images of a mouse bearing TNB tumor obtain before injection of the $NaDyF_4$-$NaGdF_4$ contrast agent: (A) T_1-weighted (TC* = 1.15 ± 0.02). *(B) T_2-weighted (TC* = 0.33 ± 0.06). *(C) Image obtained by the subtraction of (B) from (A) (TC* = 1.52 ± 0.03). *The ROI*

encompassing the tumor and tissues were manually selected and are marked with yellow and blue color respectively (in (A) only for clarity).

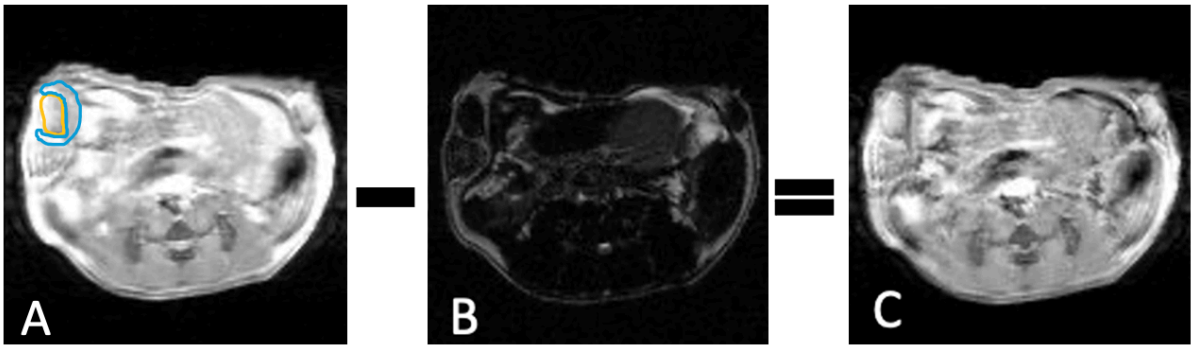

Fig. 37. *MR images of a mouse bearing with TNB tumor obtained 15 min post-injection of the $NaDyF_4$-$NaGdF_4$ contrast agent: (A) T_1-weighted (TC = 1.24 ± 0.02). (B) T_2-weighted (TC = 0.32 ± 0.07). (C) Image obtained by the subtraction of (B) from (A) (TC = 1.56 ± 0.02). The ROI encompassing the tumor and tissues were manually selected and marked with yellow and blue color respectively (in (A) only for clarity).*

The TC values pre-injection of the $NaDyF_4$-$NaGdF_4$ contrast agent into a mouse bearing TNB cancer were 1.15 ± 0.02 and 0.33 ± 0.06 for T_1w, and T_2w images respectively, while TC was equal to 1.52 ± 0.03 for subtracted T_1w − T_2w images (Fig. 36). The corresponding values post-injection were: 1.24 ± 0.02 for T_1w image, 0.32 ± 0.07 for T_2w and 1.56 ± 0.02 for the subtracted T_1w - T_2w images (Fig 37).

Table 3 provides values of S_{tu}, S_{ti}, and the TC before and 15 minutes after the injection of the $NaDyF_4$-$NaGdF_4$ contrast agent within the ROIs shown in Figure 36 and 37.

		S_{tu}	**S_{ti}**	**TC**
Pre-injection	T_1w	187.0 ± 15.2	162.0 ± 37.4	1.15 ± 0.02
	T_2w	20.0 ± 6.6	60.9 ± 22.9	0.33 ± 0.06
	T_1w − T_2w	167.0 ± 16.9	110.0 ± 32.1	1.52 ± 0.03
Post T_1/T_2 contrast injection	T_1w	230.0 ± 17.6	186.0 ± 26.9	1.24 ± 0.02
	T_2w	18.6 ± 8.2	57.6 ± 27.3	0.32 ± 0.07
	T_1w − T_2w	216.0 ± 24.5	138.0 ± 27.0	1.56 ± 0.02

Table 3. *The values of S_{tu}, S_{ti}, and TC pre- and 15 min post-injection of $NaDyF_4$-$NaGdF_4$ contrast agent obtained from the images in Figures 37 and 38. The highest TC was observed in subtracted images both before and after injection.*

In summary, the analysis of Figures 36 and 37 and the results presented in Table 3, show that application of an image subtraction can further improve the contrast between the tumor and adjacent tissue beyond the action of a contrast agent alone.

Chapter 6. Discussion and Conclusions

This thesis presents MRI investigations of H_2N-Fe_3O_4 and $NaDyF_4$-$NaGdF_4$ nanoparticles used as contrast agents for *in vivo* models of prostate cancer (PC3) and triple negative breast (TNB) cancer. The changes of the relaxation times and signal intensity measurements after contrast agents injection were performed. Furthermore, *in vivo* image post-processing applied to *in vivo* images was applied to further improve tumour contrast. The results showed improved diagnostic capability of prostate and breast cancer MRI.

The relaxivity measurements of H_2N-Fe_3O_4 contrast agent obtained in aqueous solutions showed that r_1 relaxivity was higher at 3T ($r_1 = 0.44 \pm 0.014$ $mM^{-1}s^{-1}$) than at 9.4T ($r_1 = 0.11 \pm 0.02$ $mM^{-1}s^{-1}$) while r_2 values at 3T ($r_2 = 3.0 \pm 0.8$ $mM^{-1}s^{-1}$) and 9.4T ($r_2 = 3.8 \pm 0.5$ $mM^{-1}s^{-1}$) remained similar at both field strengths. The r_1 relaxivity of $NaDyF_4$-$NaGdF_4$ nanoparticles was higher at 3T ($r_1 = 20.2 \pm 0.4$ $mM^{-1}s^{-1}$) than at 9.4T ($r_1 = 9.4 \pm 0.2$ $mM^{-1}s^{-1}$) while the values of r_2 were higher at 9.4T ($r_2 = 144.7 \pm 7.3$ $mM^{-1}s^{-1}$) than at 3T ($r_2 = 32.3 \pm 0.5$ $mM^{-1}s^{-1}$). These results showed that both H_2N-Fe_3O_4 and NaDyF4-NaGdF4 are more effective as a T_1 contrast at the lower 3T field strength than at 9.4T. These results show potential applications of the NPs for clinical MRI at 3T as strong T_1 contrast agents. The results also showed that for both nanoparticles, r_2 is higher at 9.4T hence less efficient at 3T as T_2 contrast agents.

In vivo studies showed that both NPs in both animal models produced significant enhancement of tumor contrast, specifically shortly after injection. This rapid onset of the change is attributed mostly to the EPR effect, which allows contrast agents to accumulate passively within tumours due to their irregular vasculature and impaired drainage. Importantly, these effects diminished the 2 and 24 hrs after injection, as observed the signal intensities and relaxation times returned to the initial values. This pattern suggests that the agents provide effective contrast shortly after administration, but they are washed out from the system within 2 hrs, reducing the likelihood of long-term retention and associated toxicity. At the same time, relaxation times and signal intensities in the normal tissue reduced less at each time point, implying a degree of tumour specificity in the agent's distribution.

The presented post-processing method and its application to *in vivo* MRI demonstrated that it provides additional improvement in tumor contrast. This approach is particularly effective when the contrast agent causes a strong increase in T_1-weighted signal and a strong decrease in T_2-weighted signal within the tumor region, namely the contrast agent is more efficient. In this scenario, the combined subtraction image results in the highest TC, making it a useful tool for enhancing visibility when dual-mode (core-shell) contrast agents are used.

This post-processing could be particularly relevant in clinical settings where contrast agents could be used in lower concentrations to obtained desired contrast further reducing potential toxicity. Furthermore, this method could be used for other types of cancer.

In summary, the presented research shows that both H_2N-Fe_3O_4 and $NaDyF_4$-$NaGdF_4$ contrast agents along with the image post-processing enhance diagnostic capability of MRI in prostate and breast cancer detection offering strategies for future clinical applications.

Chapter 7. Future Directions

The findings presented in this thesis highlight both the potential and the limitations of the applied contrast agents. While the studies demonstrated significant enhancement of tumor contrast, the degree of specificity and contrast retention remain areas of further improvements. These could be achieved by the integration of active targeting strategies to enhance tumor-specific uptake. Functionalizing the nanoparticle surface with ligands that bind selectively to markers commonly overexpressed in tumor, could improve accumulation in malignant tissue hence provide tumor higher contrast.

The physical and chemical properties of nanoparticles have a huge impact on their magnetic properties, hence behaviour as a contra agent. Modifying the size and composition of the shell and core could improve their relaxivities. As such, continued exploration of core and surface parameters may yield nanoparticles with improved *in vivo* behaviour and more effective contrast properties.

Another factor that should be considered is the concentration of nanoparticles administered. Increasing the amount of contrast agent delivered could improve local accumulation, strongly shortening relaxations, enhance signal differences on T_1- and T_2-weighted images, and reveal effects that were not detectable at lower doses. Future experiments should explore whether dose escalation leads to more pronounced imaging results while ensuring that biocompatibility, toxicity and clearance remain within acceptable limits.

In summary, these considerations highlight the need for a comprehensive approach to nanoparticle design, that balances physical characteristics, dosage and biological interactions. While the presented *in vivo* studies were carried out in a pre-clinical setting, they provide directions for future clinical translation and the further development of advanced MRI contrast agents.

Bibliography

[1] E. M. Haacke, R. W. Brown, M. R. Thompson, and R. Venkatesan, *Magnetic Resonance Imaging: Physical Principles and Sequence Design*, New York: Wiley-Liss, 1999.

[2] Z. Liang and P. C. Lauterbur, *Principles of Magnetic Resonance Imaging: A Signal Processing Perspective*, SPIE Optical Engineering Press, 2000.

[3] C. P. Slichter, *Principles of Magnetic Resonance*, 3rd ed. Berlin, Germany: Springer-Verlag, 1990.

[4] A. Abragam, *The Principles of Nuclear Magnetism*, Oxford, U.K.: Clarendon Press, 1961.

[5] F. Bloch, W. W. Hansen, and M. Packard, "The Nuclear Induction Experiment," *Physical Review*, vol. 70, no. 7–8, pp. 474–485, 1946.

[6] H. An, and W. Lin, "Spin Density, T1, T2, T2* Relaxation and Bloch Equations,"Curr. Protoc. Essent. Lab. Tech., vol. 00, no. 1, pp. B3.1.1–B3.1.10, 2001.

[7] G. B. Chavhan, P. S. Babyn, P. Thomas, B. Shroff, and E. M. Haacke, "Principles, Techniques, and Applications of T2*-based MR Imaging and Its Special Applications," Radiographics, vol. 29, no. 5, pp. 1433–1449, 2009.

[8] A. C. Venu, R. N. Din, T. Rudszuck, P. Picchetti, P. Chakraborty, A. K. Powell, S. Kramer, G. Guthausen, and M. Ibrahim, "NMR Relaxivities of Paramagnetic Lanthanide-Containing Polyoxometalates," Molecules, vol. 26, no. 24, p. 7481, 2021.

[9] G. K. Das, N. J. J. Johnson, J. Cramen, B. Blasiak, P. Latta, B. Tomanek, and F. C. J. M. van Veggel, "$NaDyF_4$ Nanoparticles as T_2 Contrast Agents for Ultrahigh Field Magnetic Resonance Imaging," J. Phys. Chem. Lett., vol. 3, no. 4, pp. 524–529, Feb. 2012.

[10] H. Kato, Y. Kanazawa, M. Okumura, A. Taninaka, T. Yokawa, and H. Shinohara, "Lanthanoid Endohedral Metallofullerenols for MRI Contrast Agents," J. Am. Chem. Soc., vol. 125, no. 14, pp. 4391–4397, 2003.

[11] P. Caravan, M. T. Greenfield, and J. W. M. Bulte, "Molecular Factors That Determine Curie Spin Relaxation in Dysprosium Complexes," Magn. Reson. Med., vol. 46, no. 5, pp. 917–922, 2001.

[12] K. Kattel, J. Y. Park, W. Xu, H. G. Kim, E. J. Lee, B. A. Bony, W. C. Heo, J. J. Lee, S. Jin, J. S. Baeck, Y. Chang, T. J. Kim, J. E. Bae, K. S. Chae, and G. H. Lee , ""A facile synthesis, in vitro and *in vivo* MR studies of D-glucuronic acid-coated ultrasmall Ln_2O_3 (Ln = Eu, Gd, Dy, Ho, and Er) nanoparticles as a new potential MRI contrast agent," ACS. Appl., vol. 3, pp. 3325-3334, 2011.

[13] Y.-X. J. Wang, "Superparamagnetic iron oxide based MRI contrast agents: Current status of clinical application," QIMS., vol. 1, no. 1, pp. 35–40, 2011.

[14] M. Rohrer, H. Bauer, J. Mintorovitch, M. Requardt, and H.-J. Weinmann, "Comparison of magnetic properties of MRI contrast media solutions at different magnetic field strengths," Invest. Radiol., vol. 40, no. 11, pp. 715–724, 2005.

[15] L. P. Panych and B. Madore, "The physics of MRI safety," J. Magn. Reson., vol. 47, no. 1, pp. 28–43, 2018.

[16] S. S. Hidalgo-Tobon, "Theory of gradient coil design methods for magnetic resonance imaging," Concepts in Magnetic Resonance Part A, vol. 36A, no. 4, pp. 223–242, 2010.

[17] Q. Fan, C. Eichner, M. Afzali, L. Mueller, C. M. W. Tax, M. Davids, M. Mahmutovic, B. Keil, B. Bilgic, K. Setsompop, H.-H. Lee, Q. Tian, C. Maffei, G. Ramos-Llordén, A. Nummenmaa, T. Witzel, A. Yendiki, Y.-Q. Song, C.-C. Huang, C.-P. Lin, and S. Y. Huang ., "Mapping the human connectome using diffusion MRI at 300 mT/m gradient strength: Methodological advances and scientific impact," NeuroImage., vol. 254, p. 118958, 2022.

[18] D. I. Hoult, and R. E. Richards, "The signal-to-noise ratio of the nuclear magnetic resonance experiment," J. Magn. Reson., vol. 24, no. 1, pp. 71–85, 1976.

[19] R. R. Ernst, and W. A. Anderson, "Application of Fourier transform spectroscopy to magnetic resonance," RSI., vol. 37, no. 1, pp. 93–102, 1966.

[20] P. C. Lauterbur, "Image formation by induced local interactions: examples employing nuclear magnetic resonance," Nature., vol. 242, no. 5394, pp. 190–191, 1973.

[21] M. Akcakaya, M. Tang, and R. Nezafat, "Cardiac Magnetic Resonance Imaging Physics," in Cardiovascular Magnetic Resonance Imaging, 2nd ed., L. M. Boxt and M. J. Lipton, Eds. New York, NY, USA: Springer, pp. 1–16, 2019.

[22] A. Majumdar, and R. K. Ward, Eds., MRI: Physics, Image Reconstruction, and Analysis. Boca Raton, FL, USA: CRC Press, 2015.

[23] M. A. Bernstein, K. F. King, and X. J. Zhou, Handbook of MRI Pulse Sequences. Burlington, MA, USA: Elsevier Academic Press, 2004.

[24] E. L. Hahn, "Spin echoes," Phys. Rev., vol. 80, no. 4, pp. 580–594, 1950.

[25] J. Hennig, A. Nauerth, and H. Friedburg, "RARE imaging: A fast imaging method for clinical MR," J. Magn. Reson., vol. 3, no. 6, pp. 823–833, 1986.

[26] S. H. Heywang, G. Koebrunner, and M. W. Bauer, "Analysis of the signal intensity of FLASH and FISP fast-imaging pulse sequences,"Fradi., vol. 6, 1989.

[27] R. Deichmann, and A. Haase, "Quantification of T1 values by SNAPSHOT-FLASH NMR imaging," J. Mag. Reson., vol. 96, no. 3, pp. 608–612, 1992.

[28] I. Solomon, "Relaxation processes in a system of two spins," Phys. Rev.., vol. 99, no. 2, pp. 559–565, 1955.

[29] A. K. Gupta, and M. Gupta, "Synthesis and surface engineering of iron oxide nanoparticles for biomedical applications," Biomater. Sci., vol. 26, no. 18, pp. 3995–4021, Jun. 2005.

[30] H. Nakamura, N. Ito, F. Kotake, Y. Mizokami, and T. Matsuoka, "Tumor-detecting capacity and clinical usefulness of SPIO-MRI in patients with hepatocellular carcinoma," J. Gastroenterol., vol. 35, no. 11, pp. 849–855, 2000.

[31] H. B. Na, I. C. Song, and T. Hyeon, "Inorganic nanoparticles for MRI contrast agents," Adv. Mater., vol. 21, no. 21, pp. 2133–2148, 2009.

[32] V. M. Runge, "Safety of approved MR contrast media for intravenous injection," J. of Mag, Reson., vol. 12, no. 2, pp. 205–213, 2000.

[33] Z. Zhou, and L. Z. Zhou, "Gadolinium-based contrast agents for magnetic resonance cancer imaging," Wiley Interdiscip. Rev. Nanomed. Nanobiotechnol., vol. 5, no. 1, pp. 1–18, 2013.

[34] K. Lu, R. Zhang, H. Wang, C. Li, Z. Yang, K. Xu, X. Cao, N. Wang, W. Cai, J. Zeng, and M. Gao, "PEGylated ultrasmall iron oxide nanoparticles as MRI contrast agents for vascular imaging and real-time monitoring," ACS. Nano., vol. 19, no. 3, pp. 3519–3530, 2025.

[35] W. Xue, Y. Liu, N. Zhang, Y. Yao, P. Ma, H. Wen, S. Huang, Y. Luo, and H. Fan, "Effects of core size and PEG coating layer of iron oxide nanoparticles on the distribution and metabolism in mice," Int. J. Nanomed., vol. 13, pp. 4485–4497, 2018.

[36] B. Blasiak, D. MacDonald, K. Jasinski, F.-Y. Cheng, and B. Tomanek, "Application

of H_2N-Fe_3O_4 nanoparticles for prostate cancer magnetic resonance imaging in an animal model," Int. J. Mol. Sci., vol. 25, no. 19, p. 10334, 2024.

[37] A. Stankiewicz, D. MacDonald, B. Blasiak, A. Kasparek, B. Tomanek, F.-Y. Cheng, and D. Kruk, "^{1}H Spin–Lattice Relaxation Processes in Solutions of H_2N–Fe_3O_4 Nanoparticles: Insights from NMR Relaxometry," J. Phys. Chem. B., vol. 128, no. 11, pp. 2773–2781, 2024.

[38] M. Norek, and J. A. Peters, "MRI contrast agents based on dysprosium or holmium," Prog. Nucl. Magn. Reson. Spectrosc., vol. 59, no. 1, pp. 64-82, 2011.

[39] G. H. Yue, H. P. Jia, J. A. Huang, S. L. Li, A. M. Wang, Y. C. Chen, H. L. Liu, and L. S. Zhang, "New class of efficient T_2 magnetic resonance imaging contrast agent: Carbon-coated paramagnetic dysprosium oxide nanoparticles," J. Pharm., vol. 13, no. 10, p. 312, Oct. 2020.

[40] S. Abaei, A. Tarighatnia, A. Mesbahi, and A. Aghanejad, "Antibody conjugates as CT/MRI theranostics for diagnosis of cancers: A review of recent trends and advances," Sens. Diagn., vol. 3, no. 9, pp. 1428–1441, Aug. 2024.

[41] K. Chatterjee, S. Sarkar, K. J. Rao, and S. Paria, "Core/shell nanoparticles in biomedical applications," Adv. Colloid. Interface. Sci., vol. 209, pp. 8–39, 2014.

[42] H. Zhang, J. Li, Y. Hu, M. Shen, X. Shi, and G. Zhang, "Folic acid-targeted iron oxide nanoparticles as contrast agents for magnetic resonance imaging of human ovarian cancer," J. Ovarian Res., vol. 9, no. 1, p. 19, 2016.

[43] X. H. Peng et al., "Targeted magnetic iron oxide nanoparticles for tumor imaging and therapy," Int. J. Nanomedicine, vol. 3, no. 3, pp. 311–321, 2008.

[44] J. Qiao, S. Li, L. Wei, J. Jiang, R. Long, H. Mao, L. Wei, L. Wang, H. Yang, H. E. Grossniklaus, Z.-R. Liu, and J. J. Yang, "HER2-targeted MRI contrast agent for breast cancer imaging," ACS. Appl. Mater. Interfaces., vol. 6, no. 5, pp. 3427–3432, 2014.

[45] B. Blasiak, P. L. Ferguson, V. A. Dash, B. Tomanek, and F. C. van Veggel, "Target-specific magnetic resonance imaging of human prostate adenocarcinoma using $NaDyF_4$–$NaGdF_4$ core–shell nanoparticles," ACS. Appl. Mater. Interfaces, vol. 13, no. 21, pp. 24345–24355, 2021.

[46] F. Sardanelli, C. Boetes, B. Borisch, T. Decker, M. Federico, F. J. Gilbert, T. Helbich, S. H. Heywang-Kobrunner, W. A. Kaiser, M. J. Kerin, R. E. Mansel, L. Marotti, L. Martincich, L. Mauriac, H. Meijers-Heijboer, R. Orecchia, P. Panizza, A. Ponti, A. D.

Purushotham, P. Regitnig, M. Rosselli Del Turco, F. Thibault, and R. Wilson"Magnetic resonance imaging of the breast: Recommendations from the EUSOMA working group," Eur. J. Cancer., vol. 46, no. 8, pp. 1296–1316, 2010.

[47] R. Pernar, "Epidemiology of Prostate Cancer," World J. Oncol., vol. 10, no. 2, pp. 63–89, 2019.

[48] H. Sung, J. Ferlay, R. L. Siegel, M. Laversanne, I. Soerjomataram, A. Jemal, and F. Bray "Global Cancer Statistics 2020: GLOBOCAN Estimates of Incidence and Mortality Worldwide," CA Cancer J. Clin., vol. 71, no. 3, pp. 209–249, 2021.

[49] L. Naji et al., “Digital rectal examination for prostate cancer screening in primary care: a systematic review and meta-analysis,” Ann. Fam. Med., vol. 16, no. 2, pp. 149–154, 2018.

[50] H. U. Ahmed, A. E.-S. Bosaily, L. C. Brown, R. Gabe, R. Kaplan, M. K. Parmar, Y. Collaco-Moraes, K. Ward, R. G. Hindley, A. Freeman, A. P. Kirkham, R. Oldroyd, C. Parker, M. Emberton, and the PROMIS Study Group, “Diagnostic accuracy of multi-parametric MRI and TRUS biopsy in prostate cancer (PROMIS): a paired validating confirmatory study,” Lancet., vol. 389, no. 10071, pp. 815–822, 2017.

[51] I. J. Powell, R. Bock, and S. Ruterbusch, “Epidemiology and pathophysiology of prostate cancer in African-American men,” Prostate, vol. 33, no. 3, pp. 160–166, 1997.

[52] B. Turkbey, P. A. Pinto, and P. L. Choyke , "Imaging techniques for prostate cancer: implications for focal therapy," Nat. Rev. Urol., vol. 6, no. 4, pp. 191–203, 2009.

[53] R. J. Hooley, K. L. Greenberg, R. M. Stackhouse, J. L. Geisel, R. S. Butler, and L. E. Philpotts, “Screening US in patients with mammographically dense breasts: initial experience with Connecticut Public Act 09-41,” Radiology, vol. 265, no. 1, pp. 59–69, 2012.

[54] M. Duffy, S. Shering, F. Sherry, E. McDermott, and N. O’Higgins, “CA 15-3: a prognostic marker in breast cancer,” Int. J. Biol. Markers., vol. 15, no. 4, pp. 330–333, 2000.

[55] F. Zugni, A. R. Padhani, D.-M. Koh, P. E. Summers, M. Bellomi, and G. Petralia, "Whole-body magnetic resonance imaging (WB-MRI) for cancer screening in asymptomatic subjects of the general population: review and recommendations," Cancer Imaging, vol. 20, no. 34, 2020.

[56] G. Trottier, "The role of dynamic contrast-enhanced MRI in prostate cancer: A review of imaging techniques and clinical applications," Cancer Imaging, vol. 11, no. 1, pp. 49–62, 2011.

[57] H. Al-Madhagi, V. Yazbik, W. Abdelwahed, and L. Alchab, "Magnetite Nanoparticle Co-precipitation Synthesis, Characterization, and Applications: Mini Review," Bio. Nano. Sci., vol. 13, no. 2, pp. 853–859, 2023.

[58] M. Vahabi, “Breast cancer screening methods: a review of the evidence,” Health Care Women Int., vol. 24, no. 9, pp. 773–793, 2003.

[59] World Health Organization, "Breast cancer," [Online]. Available: https://www.who.int/news-room/fact-sheets/detail/breast-cancer. [Accessed: May 2024].

[60] D. MacDonald, F. C. J. M. van Veggel, B. Tomanek, and B. Blasiak, "Contrast Enhancement in MRI Using Combined Double Action Contrast Agents and Image Post-Processing in the Breast Cancer Model," J. Mater., vol. 16, no. 8, Art. no. 3096, 2023.

[61] R. U. Svensson, J. M. Haverkamp, D. R. Thedens, M. B. Cohen, T. L. Ratliff, and M. D. Henry, “Slow disease progression in a C57BL/6 pten-deficient mouse model of prostate cancer,” Am. J. Pathol., vol. 179, no. 1, pp. 502–512, 2011.

[62] R. E. Hendrick, “High-quality breast MRI,” Radiol. Clin. North Am., vol. 52, no. 3, pp. 547–562, 2014.

[63] G. J. Strijkers, W. J. M. Mulder, G. A. F. van Tilborg, and K. Nicolay, “MRI contrast agents: Current status and future perspectives,” Anti-Cancer Agents Med. Chem., vol. 7, pp. 291–305, 2007.

[64] Y.-D. Xiao, R. Paudel, J. Liu, C. Ma, Z.-S. Zhang, and S.-K. Zhou, “MRI contrast agents: Classification and application (Review),” Int. J. Mol. Med., vol. 38, pp. 1319–1326, 2016.